Satellite-Derived Ocean Thermal Structure for the North Atlantic Hurricane Season

IAM-FEI PUN

Department of Atmospheric Sciences, National Taiwan University, Taipei, Taiwan

JAMES F. PRICE AND STEVEN R. JAYNE

Woods Hole Oceanographic Institution, Woods Hole, Massachusetts

(Manuscript received 10 August 2015, in final form 25 November 2015)

ABSTRACT

This paper describes a new model (method) called Satellite-derived North Atlantic Profiles (SNAP) that seeks to provide a high-resolution, near-real-time ocean thermal field to aid tropical cyclone (TC) forecasting. Using about 139 000 observed temperature profiles, a spatially dependent regression model is developed for the North Atlantic Ocean during hurricane season. A new step introduced in this work is that the daily mixed layer depth is derived from the output of a one-dimensional Price–Weller–Pinkel ocean mixed layer model with time-dependent surface forcing.

The accuracy of SNAP is assessed by comparison to 19 076 independent Argo profiles from the hurricane seasons of 2011 and 2013. The rms differences of the SNAP-estimated isotherm depths are found to be 10–25 m for upper thermocline isotherms (29°–19°C), 35–55 m for middle isotherms (18°–7°C), and 60–100 m for lower isotherms (6°–4°C). The primary error sources include uncertainty of sea surface height anomaly (SSHA), high-frequency fluctuations of isotherm depths, salinity effects, and the barotropic component of SSHA. These account for roughly 29%, 25%, 19%, and 10% of the estimation error, respectively. The rms differences of TC-related ocean parameters, upper-ocean heat content, and averaged temperature of the upper 100 m, are $\sim$10 kJ cm^{-2} and $\sim$0.8°C, respectively, over the North Atlantic basin. These errors are typical also of the open ocean underlying the majority of TC tracks. Errors are somewhat larger over regions of greatest mesoscale variability (i.e., the Gulf Stream and the Loop Current within the Gulf of Mexico).

1. Introduction

It is increasingly clear that ocean thermal structure (OTS) is an important factor controlling the intensity of tropical cyclones (TCs) (e.g., Emanuel 1999; Schade and Emanuel 1999; Shay et al. 2000; Lin et al. 2005, 2013; Walker et al. 2005; Wu et al. 2007; Goni et al. 2009; D'Asaro et al. 2014; Balaguru et al. 2015). The fundamental reason is that TCs acquire a significant fraction of their energy from the ocean via air–sea enthalpy (sensible + latent heat) fluxes, which are very sensitive to the temperature contrast at the air–sea interface (Emanuel 1986; Shay et al. 2000; Cione and Uhlhorn 2003; Lin et al. 2005, 2008, 2013; Shay and Uhlhorn 2008; Balaguru et al. 2015; Jaimes et al. 2015; Cione 2015). Under the effect of strong TC winds, the sea surface temperature (SST) will decrease as a result of vertical mixing and upwelling of colder upper-thermocline waters (Price 1981; Sanford et al. 1987; Shay et al. 1992; Jacob et al. 2000). This TC-induced SST cooling will reduce the air–sea temperature contrast and can lead to significant reduction in the TC's oceanic energy supply (Gallacher et al. 1989; Bender et al. 1993; Emanuel 1999; Schade and Emanuel 1999; Bender and Ginis 2000; Hong et al. 2000; Cione and Uhlhorn 2003; Emanuel et al. 2004; Lin et al. 2008, 2013; Cione et al. 2013; Balaguru et al. 2015). Strong SST cooling may even reverse the air–sea temperature contrast (i.e., SST $<$ air temperature), resulting in a negative heat flux that transfers energy from the atmosphere to the ocean (Lin et al. 2013; Walker et al. 2014; Balaguru et al. 2015).

For a given TC, the amplitude of the SST cooling is closely linked to upper-ocean thermal structure. All else

Corresponding author address: Dr. Iam-Fei Pun, Dept. of Atmospheric Sciences, National Taiwan University, No. 1, Sec. 4, Roosevelt Rd., Taipei 106, Taiwan.
E-mail: faye@as.ntu.edu.tw

DOI: 10.1175/MWR-D-15-0275.1

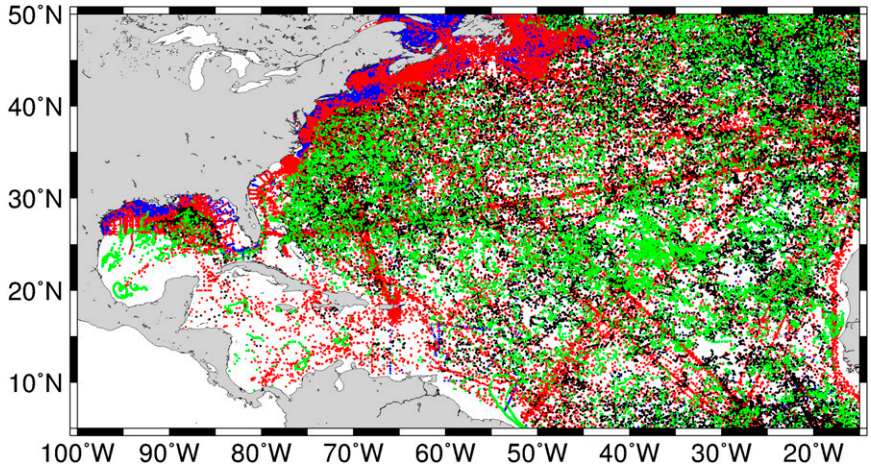

FIG. 1. Spatial distribution of the in situ temperature profiles used in this study. All data are from the North Atlantic hurricane season from June to November. Blue represents CTD profiles during 2000–10, red represents XBT profiles during 1993–2010, and black represents Argo profiles during 2000–10. These data were used to train the regression model. Green dots represent Argo profiles during 2011–13 used for validation.

being equal, less cooling is expected in regions where the pre-TC mixed layer is thick and/or the temperature gradient at the base of the mixed layer is weak (Price 1981). Thus, the TC-induced SST cooling varies regionally with OTS on a wide range of time and space scales: gyres and boundary currents (Pun et al. 2007; Lin et al. 2008, 2013; Shay and Uhlhorn 2008; D'Asaro et al. 2014), mesoscale features such as eddies and fronts (Shay et al. 2000; Lin et al. 2005; Goni et al. 2009; Jaimes and Shay 2009; Walker et al. 2014), and interannual, basin-wide phenomena such as El Niño and other long-term oscillations (Lin et al. 2008, 2014; Pun et al. 2013; Kosaka 2014). A striking example of the significant dependence of TC–ocean interaction upon OTS was reported by D'Asaro et al. (2014) who observed that Supertyphoon Megi (2010) induced 7°C of SST cooling in the South China Sea, a region characterized by a very warm and shallow surface layer, but only about 1°C in the Philippine Sea, where the western North Pacific warm pool is characterized by a very thick, weakly stratified surface layer (Ko et al. 2014). To account for the sometimes very large regional variation of TC-induced SST cooling, it is essential to have reliable OTS information available for use in TC forecasting, the goal of this study.

It has been a significant challenge to provide OTS with appropriate spatial resolution and in a timely way. Since the advent of satellite altimetry (Fu et al. 1994), there have been ongoing efforts to derive OTS from space-based observations (Carnes et al. 1990; Goni et al. 1996, 2009; Shay et al. 2000; Fox et al. 2002; Willis et al. 2003; Ali et al. 2004; Pun et al. 2007, 2014, hereafter PLK14; Shay and Brewster 2010; Guinehut et al. 2012; Wu et al. 2012; Klemas and Yan 2014; Meyers et al. 2014). Altimeters measure sea surface height anomaly (SSHA), which bears an important relation to OTS, especially the largest vertical scale of OTS variability. Based on satellite SSHA and SST measurements, PLK14 developed a regression method that aimed to provide more vertical resolution of OTS than does the widely used two-layer model (Goni et al. 1996; Shay et al. 2000; Pun et al. 2007; Shay and Brewster 2010; Meyers et al. 2014) for the western North Pacific Ocean (WNPO). The regression method of PLK14 estimates 26 isotherm depths from the sea surface to about 1000-m depth. The present study aims to extend PLK14's regression-based method with the goal of improved, operational OTS over the North Atlantic Ocean (NAO) during the hurricane season (i.e., June–November). The domain of the NAO defined here is 5°–50°N, 15°–100°W (Fig. 1). PLK14's method is upgraded with a mixed layer depth (MLD) that is computed by a one-dimensional Price–Weller–Pinkel (1D-PWP) ocean mixed layer model

TABLE 1. Numbers and periods of in situ temperature profiles used in regression model development and validation.

Type	No. of profiles	Period
Regression development		
Argo	33 464	2000–10
XBT	61 204	1993–2010
CTD	44 231	2000–10
Validation		
Argo	19 076	2011–13

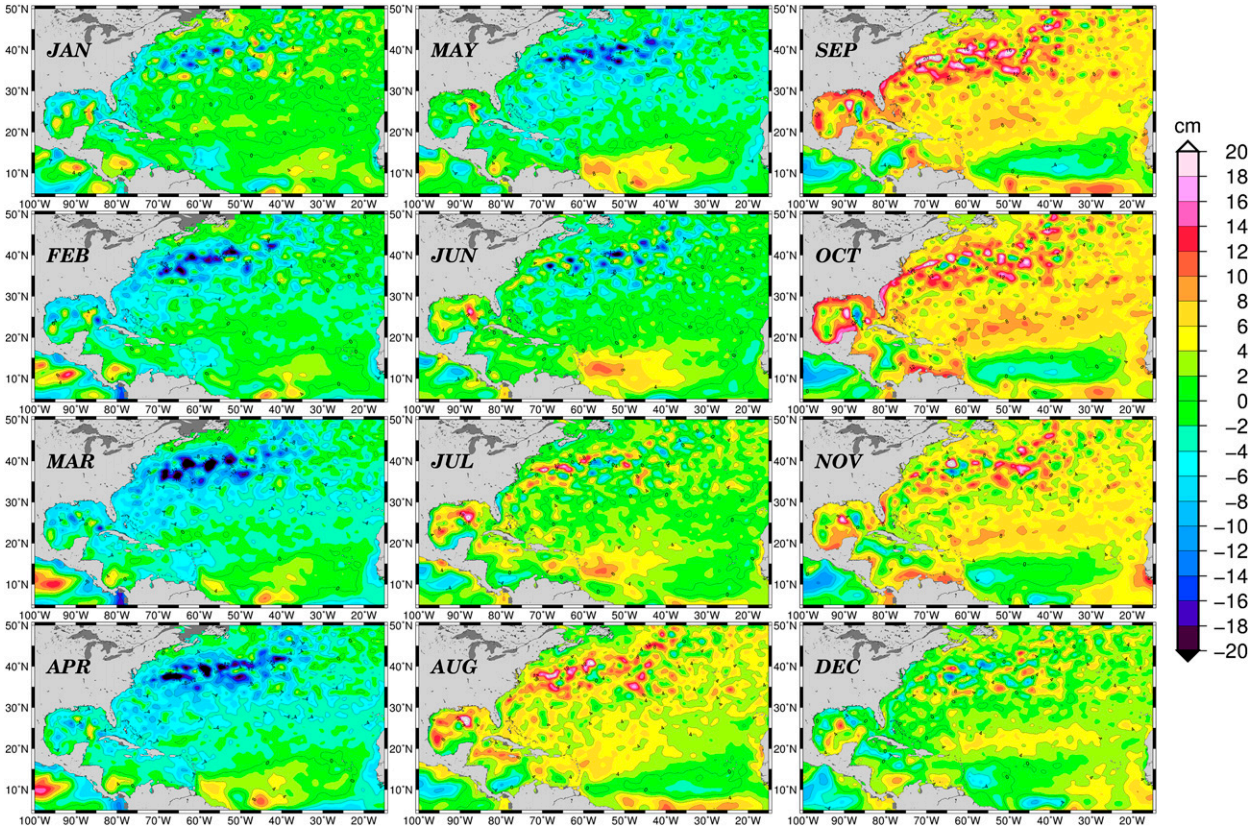

FIG. 2. Long-term-averaged monthly SSHA maps based on the daily maps from 1993 to 2010. These data are courtesy of AVISO.

(Price et al. 1986) forced by realistic wind stress and radiation fluxes. This new method is called the Satellite-derived North Atlantic Profiles (SNAP).

2. Data

A total of 157 975 in situ ocean temperature profiles were used to develop and test the new model (Table 1). These data were collected from the Argo project (Gould et al. 2004; Roemmich et al. 2004) and historical ship-based conductivity–temperature–depth (CTD) and expendable bathythermograph (XBT) observations (Fig. 1). Of these profiles, 138 899 (88%) were used to establish (train) the regression model, while 19 076 (12%) independent profiles were withheld to assess accuracy.

a. Argo profiling float data

Argo floats repeatedly measure temperature, salinity, and pressure with high vertical resolution, usually 5–10 m for the upper ocean and 50–100 m for the deeper depths, depending on the float type. The depth range of Argo measurement is typically from the surface to 2000 m. The current Argo array consists of more than 3500 floats, providing ice-free ocean temperature and salinity profiles with global coverage every 10 days, roughly.

The Argo profiles used here were downloaded from the French Research Institute for Exploitation of the Sea (IFREMER; ftp.ifremer.fr). Some 33 464 Argo profiles collected from 2000 to 2010 were used for regression development and 19 076 profiles collected from 2011 to 2013 were used to assess the accuracy of SNAP. These Argo profiles have gone through the real-time quality control test procedures and flagged as good data by the Argo Data Management Team (Wong et al. 2012).

b. Ship-based profiles: CTD and XBT

There are only a comparatively few Argo profiles in the Gulf of Mexico (GOM), the Caribbean Sea, and coastal waters generally (Fig. 1). To increase the number of profiles in those areas, ship-based CTD and XBT data were also used. These data were obtained from the *World Ocean Database 2009* (*WOD09*) (Boyer et al. 2009), distributed by the National Oceanic and Atmospheric Administration (NOAA)/National Oceanographic Data Center (NODC). All of the profiles

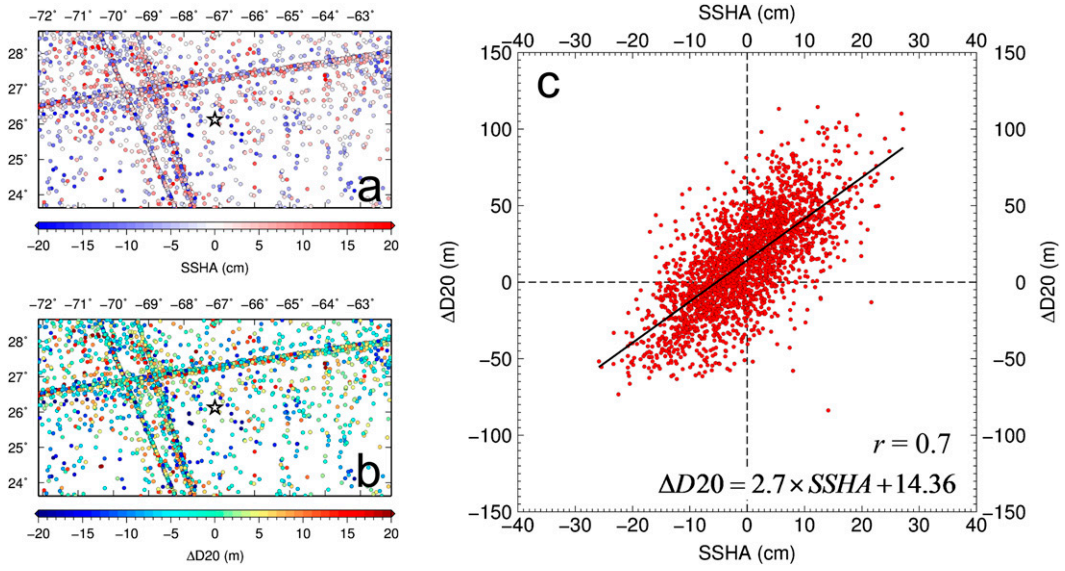

FIG. 3. (a) The 2497 profiles (color coded by corresponding SSHA) inside the 10° by 5° box centered on 26.125°N, 67.125°W (star at the middle of the box). (b) As in (a), but color coded by ΔD20, which is the difference between in situ (Argo) D20 and climatological (GDEM) D20. (c) ΔD20 vs SSHA from these 2497 profiles, based upon which a linear regression of D20 is obtained for the central grid point.

archived in WOD09 were quality controlled (Boyer et al. 2009).

A total of 44 231 CTD profiles were found during the hurricane seasons during 2000–10. Most of those profiles were located in coastal areas of the United States (Fig. 1). For XBTs, the period was extended back to 1993 when the high accurate altimetry data (e.g., from TOPEX/Poseidon) became available. There are 61 204 XBT profiles collected during the hurricane seasons during 1993–2010. It should be noted that XBT contributes most of the profiles available from coastal waters and in the Caribbean Sea, where Argo and CTD data are rather sparse.

c. *Satellite altimetric SSHA and radiometric SST*

The altimetric data used here are the daily merged and gridded SSHA maps from the Archiving, Validation, and Interpretation of Satellite Oceanographic Data (AVISO; www.aviso.altimetry.fr) data center. Sea surface height anomaly measurements from multiple altimetry missions [e.g., TOPEX/Poseidon, *Jason-1*, *Environmental Satellite* (*Envisat*), etc.] are combined together by the AVISO team (Ducet et al. 2000; Pascual et al. 2006, 2009) to generate a daily gridded field with 0.25° spatial resolution. Here the delayed time "all-sat-merged" product is used, which is expected to provide the highest quality SSHA map.

There are significant seasonal variations in the SSHA field, up to 10 cm (Fig. 2). The highest sea level occurs from September to November, while the lowest is from March to May. To be consistent with the isotherm depth anomaly calculated later, the seasonal cycle of SSHA was removed by subtracting the monthly composite average computed between 1993 and 2010.

The SST data used here are from the cloud-penetrating microwave optimally interpolated SST (OISST) analysis of the Remote Sensing Systems (RSS; www.remss.com). This product is generated by blending SST measurements from multiple microwave radiometers, which include the Tropical Rainfall Measuring Mission (TRMM) Microwave Imager (TMI), the Advanced Microwave Sounding Radiometer for the Earth Observing System (AMSR-E), AMSR2, and WindSat (Gentemann et al. 2010). The OISST dataset has 0.25° spatial resolution and is provided on a daily basis.

d. *GDEM ocean climatology*

The U.S. Naval Research Laboratory (NRL)'s Generalized Digital Environmental Model, version 3 (GDEM), monthly climatology was adopted here as the reference ocean temperature and salinity structure. The GDEM climatology has horizontal resolution of 0.25° and temporal resolution of one month. GDEM was produced with a large number of classified in situ profiles not otherwise available for this use (Carnes 2009). As pointed out by Meyers et al. (2014), a monthly climatology taken literally will show a large jump from one month to the next. For example, the corresponding climatological depth of 20°C isotherm (D20) maps for June and July shows up to ±40-m

differences. Since the profiles and the satellite data are analyzed here on a daily basis, the GDEM monthly climatology is interpolated to a daily value. By this procedure, the unphysical jump between monthly means is eliminated.

It is noteworthy that this new method is not particularly sensitive to the choice of the climatology since climatology serves merely as a reference in SNAP; the difference introduced by a specific climatology would be adjusted by the regression equation.

3. Regression model

a. Training the regressions

The development of the regression model generally follows the procedure introduced in PLK14 (viz., the model seeks to estimate isotherm depth anomaly, ΔD_k, from the observed SSHA, $\Delta\eta$):

$$\Delta D_k = a_{(i,j,k)} \times \Delta\eta_{(i,j,t)} + b_{(i,j,k)}. \quad (1)$$

The index k defines which isotherm, 29°, 28°, 27°, . . . , 4°C. The operator Δ defines the anomaly of isotherm depth or sea surface height with respect to a smoothly varying annual mean (i.e., $\Delta D_k = D_k - \overline{D_k}$) and similarly for $\Delta\eta$. The regression coefficients, a and b, are a function of location (i, j) and k, respectively; i and j are longitude and latitude, respectively, with 0.25° increment; and t is time.

The regression is computed from the profiles within a box that is nominally 10° longitude by 5° latitude centered on each 0.25° grid point. Thus, all of the ΔD_k and $\Delta\eta$ pairs located within this box are used to estimate the linear regression [Eq. (1)] for that central grid point. An exemplary regression procedure for D20 in the subtropical NAO at 26.125°N, 67.125°W is shown in Fig. 3. Within this 10° by 5° box, there were 2479 temperature profiles. In this typical example, there is a significant linear relationship between SSHA and D20 with correlation coefficient, $r = 0.7$. This regression shows that 1 cm of SSHA projects into 2.7-m depth anomaly of the 20°C isotherm, D20. Figure 4 shows the spatially varying regression coefficients (a and b) for D20 and the number of profiles available at each grid point. It is evident that the regional variation of the regression coefficients is quite significant.

In the NAO domain there are two important marginal seas—the Caribbean Sea and GOM—that have hydrographic conditions markedly different from the open NAO at the same latitude. The Caribbean Sea OTS includes a very deep warm water layer all year-round (Fig. 5a), while the GOM is dominated by the Loop Current and its eddies (Shay and Uhlhorn 2008; Goni et al. 2009). To acknowledge this difference in hydrographic conditions the profiles are separated into three basins, which are the Caribbean Sea, GOM, and open NAO (Fig. 5b). The 10° by 5° boxes do not overlap one region to the next. Notice that the profiles available for evaluating the regression in the southwestern part of the GOM and the western part of the Caribbean Sea are especially sparse (Fig. 4c).

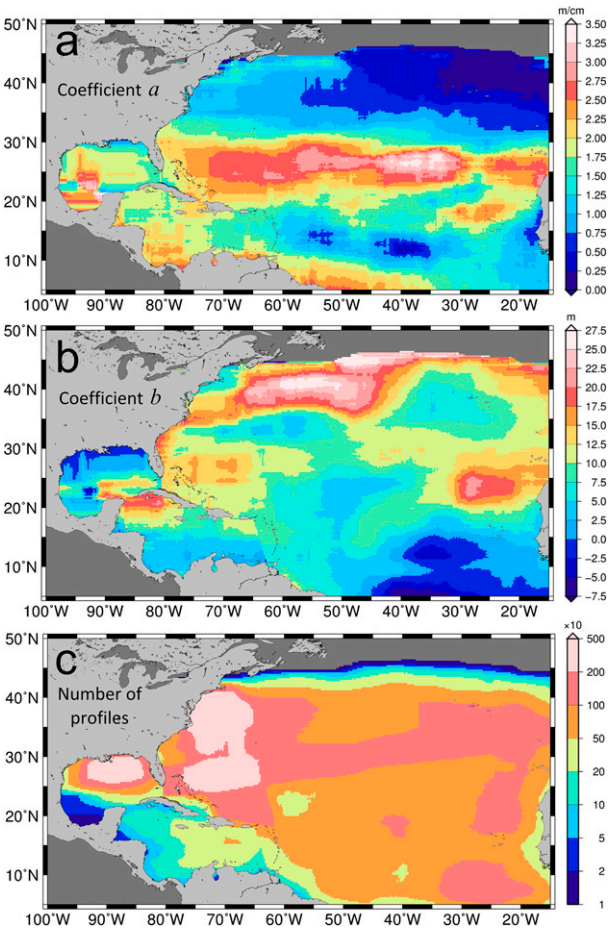

FIG. 4. (a) The D20 linear regression coefficient a, (b) coefficient b, and (c) the number of profiles used to train the regression at each grid point.

b. Correlation between SSHA and subsurface isotherms

The correlation between SSHA and the vertical displacement of the isotherm depths can be viewed as an index evaluating the goodness of the regression. Figure 6b shows the correlation between SSHA and D20, which is usually used as a proxy for the depth of the main thermocline (Goni et al. 1996; Shay et al. 2000; Pun et al. 2007). High correlation, $r = 0.6$–0.8, is found in the GOM, Caribbean Sea, and western NAO (i.e., Sargasso Sea), indicating that the derived regressions have a

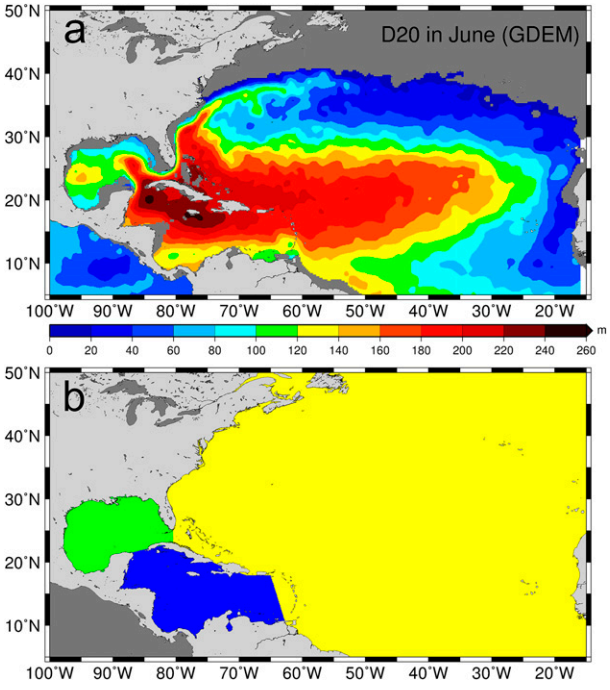

FIG. 5. (a) GDEM climatological D20 in average June. (b) Three subbasins: the Caribbean Sea (blue), GOM (green), and open NAO (yellow).

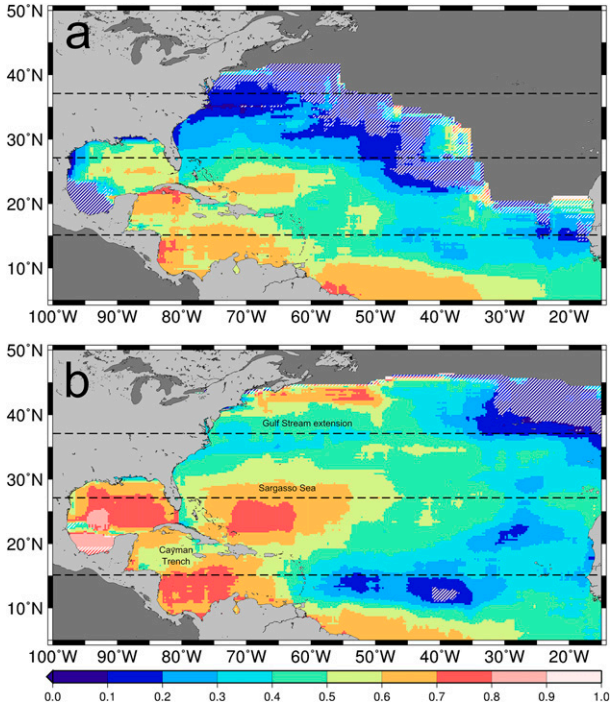

FIG. 6. Spatial distribution of correlation coefficient r between SSHA and (a) D26 and (b) D20. The areas marked with diagonals indicate that the correlation is less than 99% significant based on Student's t test. Dashed lines indicate the latitudes of the cross sections in Fig. 8 at 37°, 27°, and 15°N. The geographic locations of the Gulf Stream extension, Sargasso Sea, and Cayman Trench are noted in (b).

useful ability to estimate D20 variation from SSHA in these areas. However, relatively low correlation is found in the eastern NAO (Fig. 6b) where D20 may be within the mixed layer or even outcrop the sea surface (Fig. 5a). It is also noted that a significant low correlation patch stretches from the east of the Caribbean Sea to the western coast of Africa. Notice that this area is associated with low SSHA and high salinity variations, where the standard deviations of SSHA and salinity are only about 4 cm and >0.2 psu, respectively (Fig. 7). These two factors likely contribute to the low correlation between SSHA and the isotherm variation (more on errors below). In addition, the high eddy activity and salinity effect may also explain the low correlation between SSHA and D20 along the Gulf Stream extension area, where SSHA and salinity variations are remarkable (Figs. 6b and 7). Similar correlation pattern is found in D26 (Fig. 6a), which is often used to measure the thickness of the warm water layer (Lin et al. 2008). However, the correlation coefficient is somewhat less than that of D20. This is probably because D26 is usually closer to the base of the surface mixed layer. Interestingly, relatively low correlation is found throughout the water column along the Cayman Trench, indicating that the bottom topography may affect sea surface height behavior (i.e., more barotropic variability that is not associated with significant OTS anomaly), though it could also be related to the low number of profiles in this area (Fig. 4c).

To see how the correlation varies in the vertical, three cross sections along 37°, 27°, and 15°N latitudes are extracted roughly for the Gulf Stream, GOM, and Sargasso Sea–Caribbean Sea, respectively (Fig. 8). In the Gulf Stream (west of 35°W) high correlation ($r > 0.6$) is found in the layer between D18 and D4, whereas outside the Gulf Stream (east of 35°W) SSHA is better correlated with D14, D13, and D12 (Fig. 8a). In the GOM, SSHA mainly represents the variations in the isotherms between D25 and D5 (Fig. 8b). It is interesting that two maximum correlation peaks appear in the Sargasso Sea: one between D23 and D18 and the other at deeper depths between D12 and D5 (Fig. 8b). Strong correlation is also found in the Caribbean Sea between D27 and D8 (Fig. 8c). As aforementioned, low correlation is found in D20 and D26 at this low-latitude band (~15°N) east of the Caribbean Sea, the correlation for the whole column of isotherms is in fact less than 0.5. Clearly, there are significant regional variations of the ΔD_k–$\Delta\eta$ correlations, which the method developed here attempts to take into account.

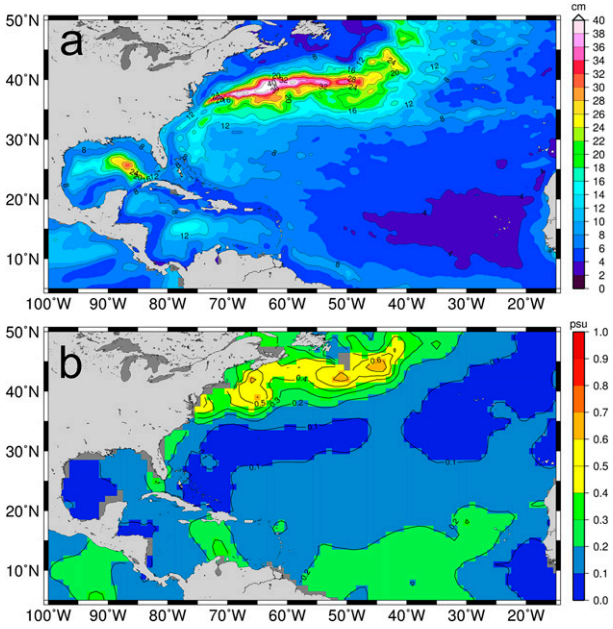

FIG. 7. (a) Standard deviation of SSHA in the North Atlantic Ocean based on the AVISO daily SSHA maps during 2001–10. (b) Standard deviation of salinity at 100-m depth during September based on GDEM salinity analysis.

4. Daily mixed layer depth

A useful estimate of OTS must include a realistic SST along with the thickness of the surface layer over which SST is relevant (Pun et al. 2007; Meyers et al. 2014). Here the surface layer thickness is identified as the thickness (or depth) of the surface isothermally mixed layer. For the sake of simplicity, this depth is hereafter referred to as MLD and its definition will be introduced later in this section. The mixed layer depth and its associated temperature make a very significant contribution to upper-ocean heat content (UOHC; Leipper and Volgenau 1972; Shay et al. 2000; Goni et al. 2009), which is commonly used in tropical cyclone research. The mixed layer depth varies rapidly (hours) with the surface fluxes (Mellor and Yamada 1982; Price et al. 1986; Kantha and Clayson 1994; Bernie et al. 2005). Pun et al. (2007) and PLK14 adopted the climatological monthly MLD from NRL (Kara et al. 2002) to complete their satellite-derived profiles. Recently, Meyers et al. (2014) attempted to improve MLD by correlating MLD with SSHA observation, just as described above for the subsurface temperature. However, there is only a weak correlation between the variables SSHA and MLD. In part, this arises because the temporal variation of MLD is much faster than the altimetry observing frequency, the former can be in hours and the latter is usually every several days even when multiple altimeters are combined together.

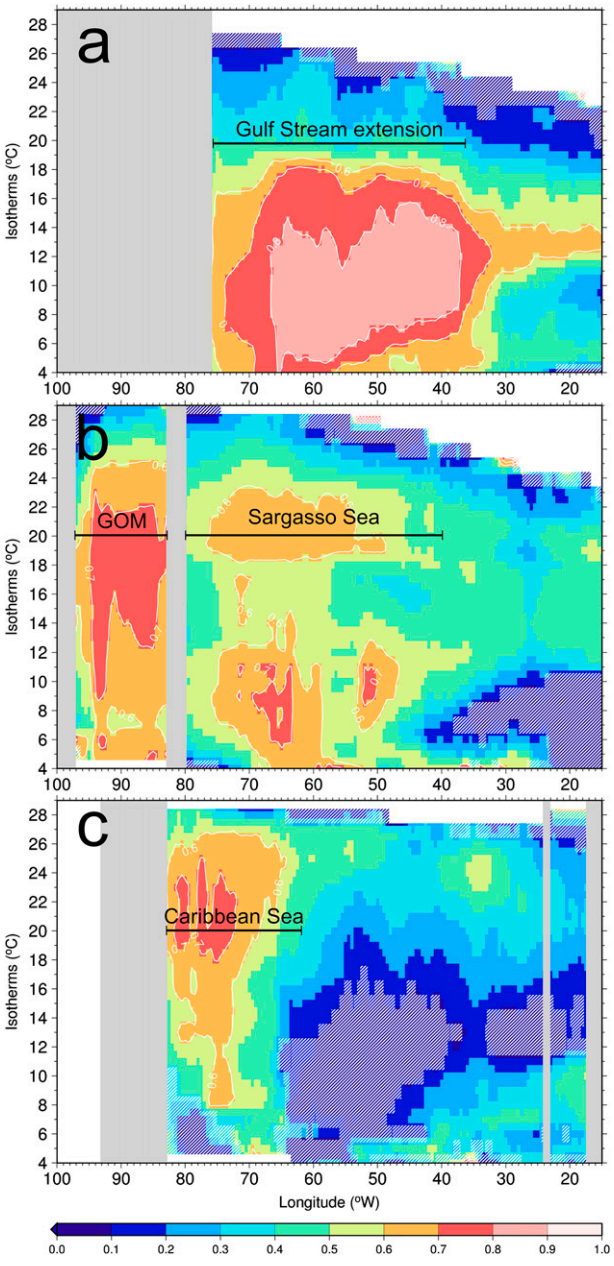

FIG. 8. SSHA–isotherm correlation cross section along (a) 37°, (b) 27°, and (c) 15°N. Gray depicts land and white surface layer indicates no correlation obtained. Diagonals indicate the correlations that are less than 99% significant. The zonal extents of the Gulf Stream extension, GOM (Gulf of Mexico), Sargasso Sea, and Caribbean Sea are noted.

1D-PWP estimation

This study aims to improve the estimation of MLD by employing a simple, one-dimensional (depth and time-dependent only) ocean mixed layer model developed by Price et al. (1986). The implicit assumption is that the short term—days to a week—variation of MLD over

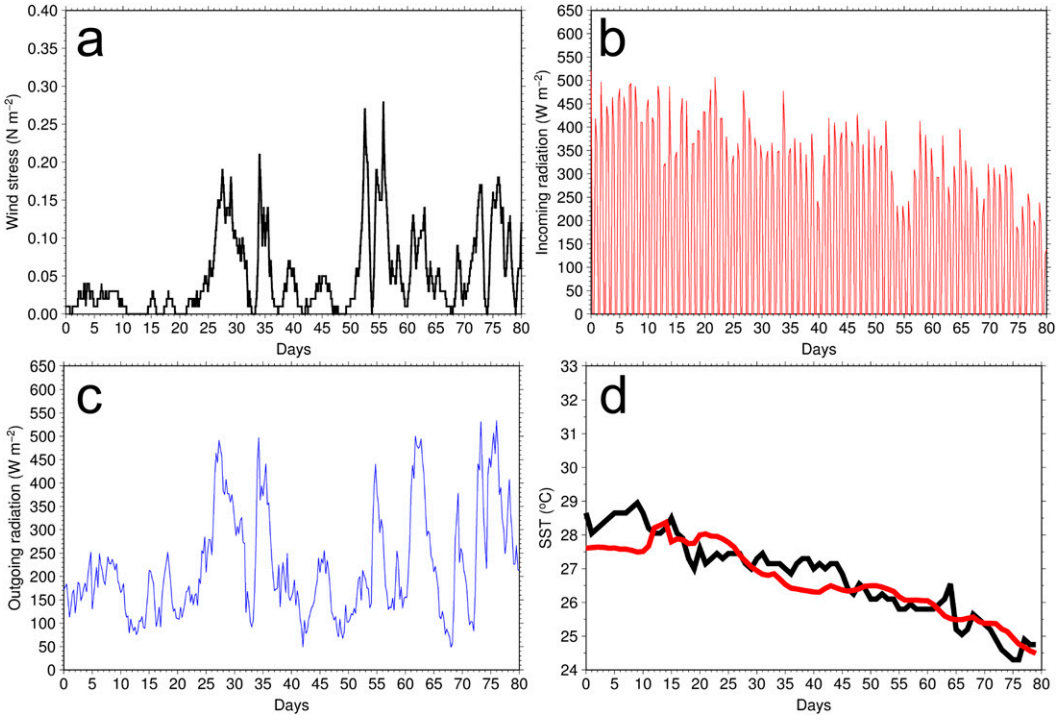

FIG. 9. Examples of the surface wind and flux data from NCEP's Reanalysis-1 used to drive the 1D-PWP model. (a)–(c) The time series of wind stress, incoming radiation (i.e., shortwave), and outgoing radiation (i.e., longwave, latent heat, and sensible heat), respectively, at 29.5°N, 68.6°W from 1 Sep to 20 Nov 2010 (i.e., 80 days). (d) Comparison between satellite-based OISST (black) and 1D-PWP-simulated SST (red). It is typically the case that the first 5–10 days of an integration show larger errors than do later times.

most of the open ocean is driven mainly by the surface fluxes. The 1D-PWP accepts as input the usual surface heat and freshwater fluxes (discussed below) and then distributes the resulting buoyancy over the upper ocean according to three mixing processes. The first process is a buoyancy (heat + freshwater) flux–induced free convection, the second and third ones are wind-driven mixed layer entrainment and vertical shear flow instability.

The initial condition, temperature and salinity profiles, is extracted from the daily climatological GDEM temperature and salinity analyses. The surface forcing terms input to the 1D-PWP includes shortwave and longwave radiations, latent and sensible heat fluxes, precipitation, and surface winds, which are extracted from the 6-hourly reanalysis fields based on Reanalysis 1 dataset of NOAA/National Centers for Environmental Prediction (NCEP). The wind stress is computed from the winds via the usual

$$\tau_x = \rho_a C_D u|U|, \quad \text{and} \tag{2}$$

$$\tau_y = \rho_a C_D v|U|, \tag{3}$$

where τ_x and τ_y are the x and y components of the wind stress, respectively; ρ_a is air density taken as 1.2 kg m^{-3}; and $|U|$ is the absolute wind speed and u and v are the east and north components, respectively, of the wind velocity. The drag coefficient, C_D, is from Powell et al. (2003), which is suitable under high wind (>25 m s^{-1}) conditions.

Examples of the surface wind stress and fluxes are in Figs. 9a–c. These are for 29.5°N, 68.6°W over a period of 80 days beginning on 1 September 2010. The initial temperature and salinity profiles at that location were based on 1 September GDEM daily climatology. The evolution of 1D-PWP-simulated SST can be compared to that of satellite-based OISST (Fig. 9d). It is found that the 1D-PWP performs fairly well insofar as the tendency of the modeled SST is in good agreement with that of satellite observation. The sea surface temperature appears to decline after 1 September 2010, coincident with the decrease in the incoming (shortwave) radiation and the increase in outgoing (longwave + latent and sensible heat fluxes) radiation (Figs. 9b,c). Note that the 1D-PWP used in this way does not simulate well SST during the first 10 days of the integration. This is common, and this is attributed to the time required for the model to adjust (or forget) the details of the initial condition. Therefore 15 days are allowed for the 1D-PWP to adjust to the surface forcing, and then compute MLD from the

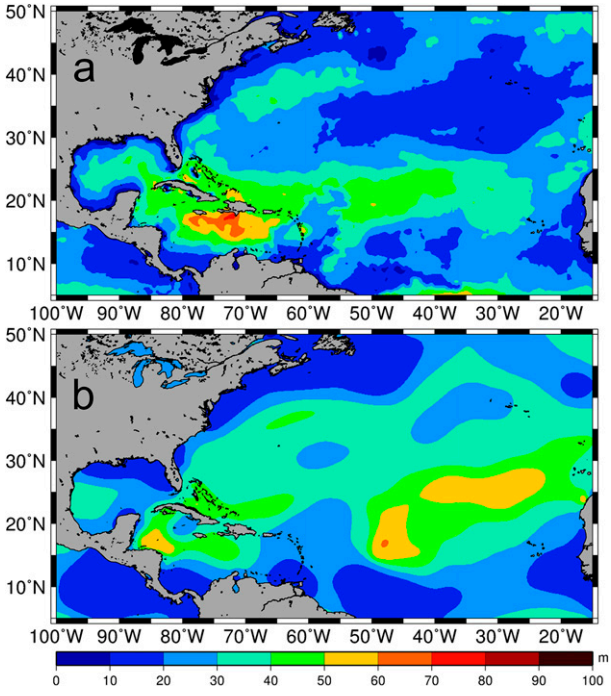

FIG. 10. Comparison between (a) 1D-PWP-derived MLD on 1 Sep 2012 and (b) NRL's September climatology of MLD.

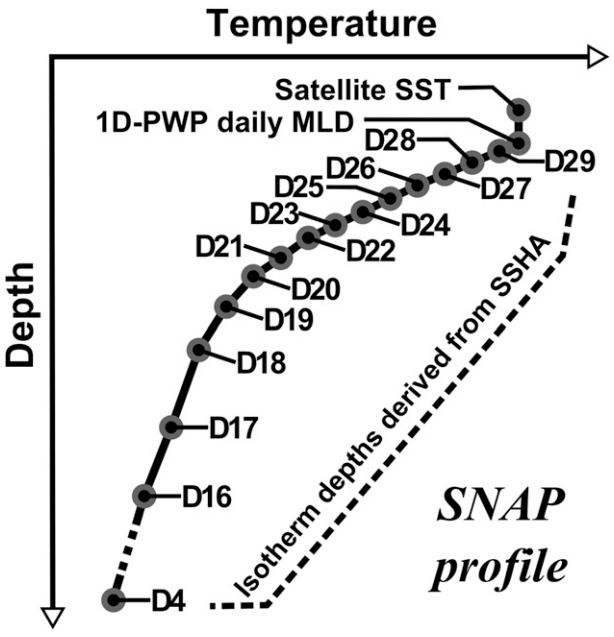

FIG. 11. Schematic of SNAP, which comprises satellite-derived SST, 1D-PWP-derived daily MLD, and up to 26 isotherm depths from altimetry SSHA based on the regression model.

simulated temperature profile. The length of 15 days is a compromise between time efficiency and accuracy based on results like that of Fig. 9d.

To obtain MLD for the entire NAO, the 1D-PWP is set to run for every 2° spatial grid for every day. The 2° MLD map is linearly interpolated into 0.25° native to SNAP. For instance, MLD on 1 September 2012 was obtained from the 1D-PWP-simulated profile based on GDEM temperature and salinity profiles on 18 August as initial conditions and the surface forcing from 18 August to 1 September 2012.

Figure 10 compares the 1D-PWP-derived MLD map on 1 September 2012 and the climatological September MLD map from NRL. The MLD was calculated from the 1D-PWP-derived profile based on a threshold of 0.3°C difference from the temperature at 10-m depth (Kara et al. 2003). Choosing the temperature at 10 m as a reference was an attempt to avoid the largest amplitude of the diurnal fluctuations that occurs in the modeled profile. It is evident that the MLD patterns are rather different: in the 1D-PWP-derived map, the thickest MLD (60–80 m) is located in the Caribbean Sea, while in the climatology the thickest MLD is located in the central NAO.

Given an estimate of MLD and satellite-derived SST, together with up to 26 isotherm depths (i.e., D29–D4) derived from SSHA based on the regression model developed in section 3, the end result is a temperature profile (OTS) that can be obtained at 0.25° spatial resolution on a daily basis (Fig. 11). A validation of this SNAP-derived OTS is described in the next section.

5. Validation

All of the Argo temperature profiles collected from 2011 to 2013 during the hurricane season (from June to November, 19 076 in total) were withheld from the training stage and are here used to assess the accuracy of SNAP (Fig. 1 and Table 1). Validations will be performed for the isotherm depths, D20, D26, the 1D-PWP-derived daily MLD and two hurricane-related ocean parameters: UOHC and vertically averaged temperature of upper 100 m, T100 (Price 2009).

a. Regression-derived isotherm depths

Isotherm depths, which are derived from SSHA via the regression model, are the essential components making up SNAP (Fig. 11). In particular, D20 and D26 have long been used to characterize the depth of the main thermocline and the thickness of surface warm water layer (e.g., Goni et al. 1996; Shay et al. 2000; Lin et al. 2005, 2008, 2009). It is noteworthy that the profiles available for D20 validation is about 1.5-fold the profiles used for D26 validation because many of the profiles located in the northern NAO have SST < 26°C and hence do not contain D26. Comparing to the Argo observations, it is found that the regression model is able to derive reliable D20 and D26 from altimetry SSHA for the NAO overall with

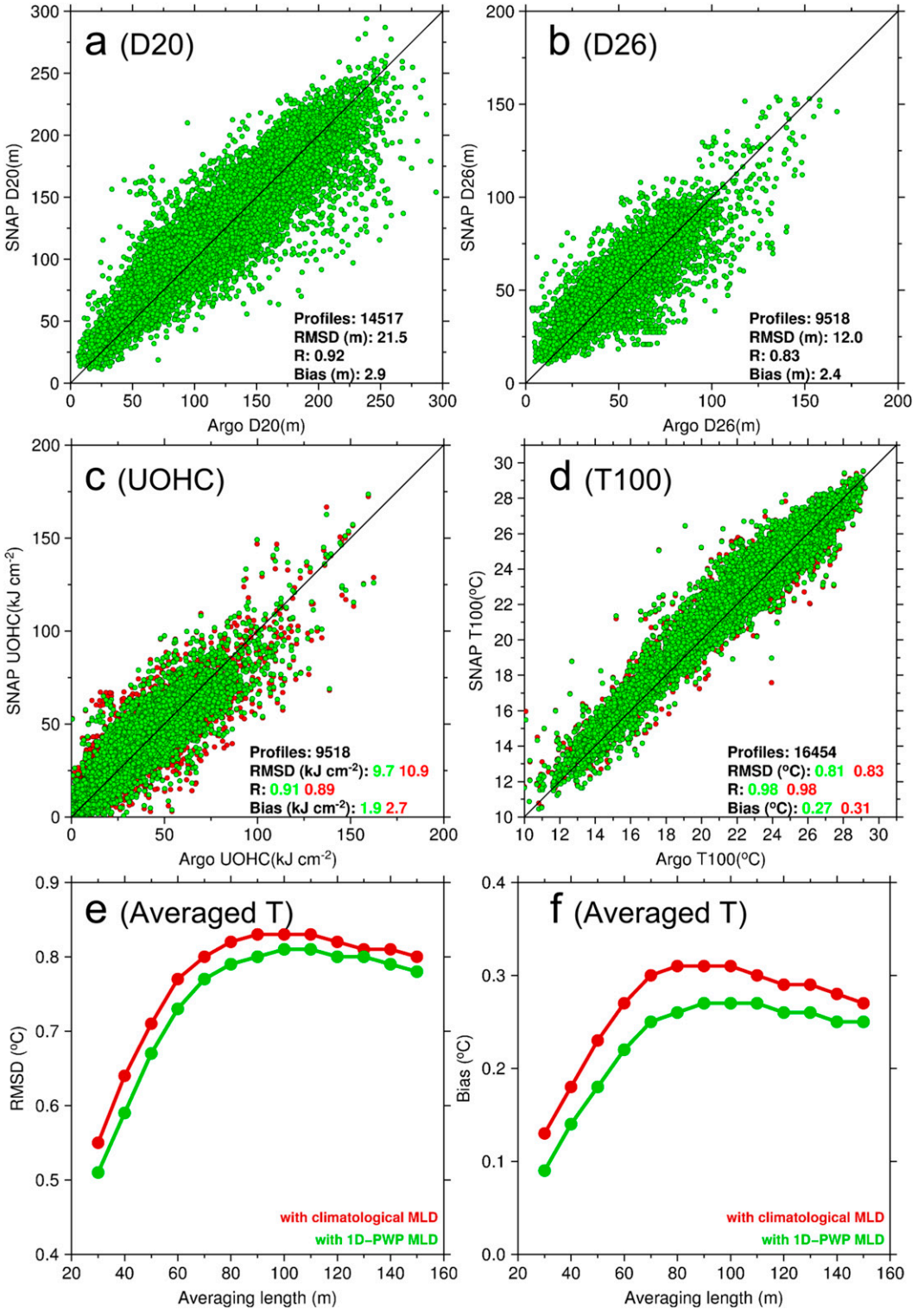

FIG. 12. Scatterplots of SNAP estimations against Argo observations over the entire NAO domain (Fig. 1) for the test period: (a) D20, (b) D26, (c) UOHC, and (d) T100. In (c) and (d) scatterplots that compare the results from the use of climatological MLD (red) and nominal SNAP, using 1D-PWP-derived MLD (green) are also shown. Sample number, RMSD, correlation, and bias with respect to Argo are shown in each scatterplot. (e),(f) RMSDs and biases for averaged temperatures (T30–T150) using different averaging lengths ranging from 30 to 150 m.

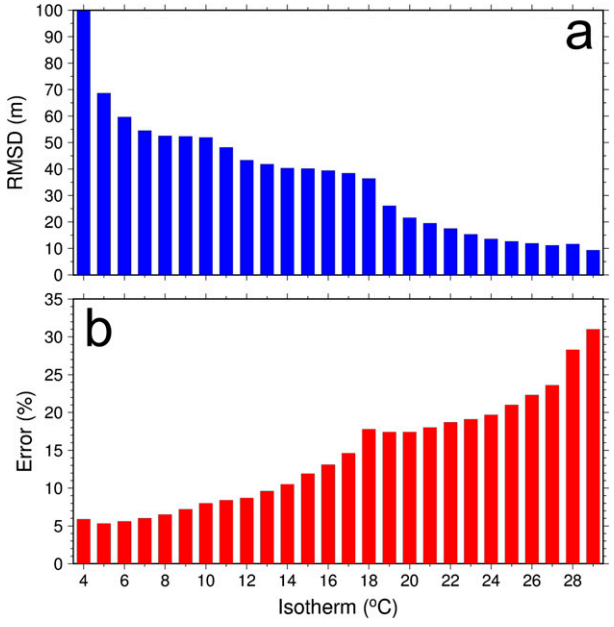

FIG. 13. (a) NAO-wide rms difference and (b) error percentage of regression-derived isotherm depths from D29 to D4. The error percentage is RMSD normalized with the rms of observed depth.

r = 0.92 and 0.83, respectively (Figs. 12a,b). The root-mean-squared (rms) differences (RMSDs) of D20 and D26 with respect to the Argo observations are 22 and 12 m, respectively, and no significant biases are found.

Figure 13 shows RMSD and the error percentage for all regression (SSHA)-derived isotherm depths from D29 to D4. The rms difference increases with isotherm depths; RMSD is about 10–25 m for upper isotherms (D29–D19), 35–55 m for the middle isotherms (D18–D7), and increases from 60 to 100 m at the lower isotherms (D6–D4). The error percentage is RMSD normalized with the rms of observed depth. The error is generally within 30% for all isotherms. The error sources for SNAP-derived isotherm depth estimations will be discussed in a later section 6b.

b. 1D-PWP-derived MLD

The collocated and coincident 1D-PWP-derived MLD is extracted for each Argo profile for the comparison. The mixed layer depth of the Argo profiles (hereafter Argo_MLD) is calculated with the temperature criterion introduced in section 4. In addition to comparing with the Argo_MLD, the NRL's climatology monthly MLD (hereafter NRL_MLD) is also used for a reference. The definition of NRL_MLD is based on density criterion that takes the salinity into account, but still depends mainly upon temperature change (Kara et al. 2002).

The intercomparisons between 1D-PWP-derived MLD, NRL_MLD, and Argo_MLD during the NAO's hurricane season are shown in Fig. 14. Although the 1D-PWP-derived MLD versus Argo_MLD is quite scattered, the tendency agrees with Argo observations and in general, 1D-PWP-derived MLD outperforms the climatological NRL_MLD for all months from June to November. Interestingly, it is found that the NRL_MLD seems to have a cap value. For example, NRL_MLD saturates at ~50 and ~60 m in September and October, respectively. In contrast, the 1D-PWP roughly estimates the early fall increase in MLD, especially in October. The monthly statistics are summarized in Table 2. On average, RMSD between 1D-PWP-derived MLD and Argo_MLD is ~13 m, with the lowest error (~9 m) in August and the highest error (~18 m) in November. The rms difference for NRL_MLD is ~15 m, also with the lowest (~11 m) in August and the highest (~21 m) in November. The overall improvement of 1D-PWP-derived MLD over NRL_MLD is 14%–24% depending upon month, showing that the present use of the 1D-PWP has some efficacy, at least compared with the use of a climatology.

c. Vertically integrated parameters: UOHC and T100

UOHC defines the heat content that exceeds 26°C:

$$\mathrm{UOHC}_{(x,y)} = c_p \rho \sum_{z=0}^{\mathrm{D26}} \Delta T_{(x,y,z)} \Delta Z, \tag{4}$$

where c_p is the heat capacity of the seawater at the constant pressure, 4178 J kg^{-1} °C^{-1}; ρ is the density of seawater, 1026 kg m^{-3}; and ΔT is the difference between $T(z)$ and 26°C over the depth interval ΔZ (Leipper and Volgenau 1972). UOHC is widely used to characterize the upper-ocean energy available for TC's intensification (Shay et al. 2000; Goni et al. 2009; Mainelli et al. 2008; Lin et al. 2009). Recently, Price (2009) proposed that a vertical average of ocean temperature may have better properties than does the integral [Eq. (4)] especially in shallow or cold waters (Lin et al. 2013, 2014; D'Asaro et al. 2014; Balaguru et al. 2015). The appropriate depth of the averaging (i.e., the depth to which vertical mixing reaches) depends significantly upon ocean stratification and upon TC intensity and translation speed (Price 2009; Lin et al. 2013; Balaguru et al. 2015). The aim here is to characterize ocean-only properties, and hence this validation will focus on T100 (i.e., averaging length = 100 m). Both UOHC and T100 can be readily calculated from Argo and SNAP-derived profiles. The long-term goal is to nowcast these parameters with an accuracy of 5 kJ cm^{-2} for UOHC and 0.5°C for T100, not quite reached by the present model. These values were judged to be significant to TC–ocean interaction, and within the bounds of

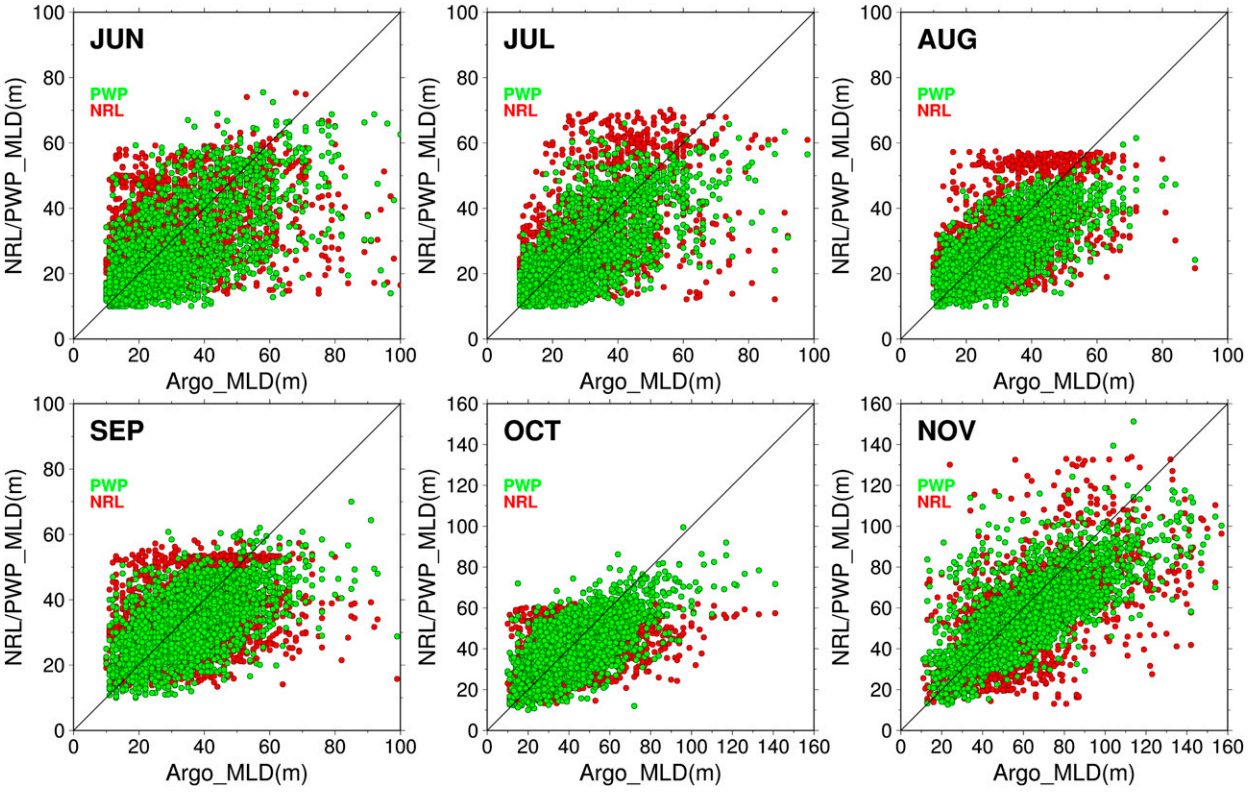

FIG. 14. Monthly MLD comparisons between 1D-PWP-derived MLD (green), NRL_MLD (red), and Argo_MLD from June to November of 2011 and 2013. Note that the scales in October and November plots are different from others.

observational and analytic errors (Cione et al. 2000; Cione and Uhlhorn 2003; Mainelli et al. 2008).

Figures 12c and 12d show the comparisons between the Argo observations and estimates from SNAP. It is evident that SNAP-derived UOHC and T100 are highly correlated with the corresponding Argo observations with $r > 0.9$. The rms differences of derived UOHC and T100 are $\sim 10\,\mathrm{kJ\,cm^{-2}}$ and ~0.8°C, respectively, and no obvious biases are found.

The error for the depth-averaged temperatures with different averaging lengths from 30 to 150 m was also evaluated (Figs. 12e,f). It is found that RMSD and bias reduce significantly as the averaging length shoals. From T100 to T30, RMSD decreases from 0.8° to 0.5°C, likely the shorter averaging lengths are often within the surface layer, where (observed) SST dominates. In addition, there are gradual decreases in RMSD and bias from T110 to T150, probably due to the benefit from the regression-derived isotherm depths.

It is noteworthy that the use of 1D-PWP-derived MLD in SNAP reduces the overall RMSD of UOHC by ~11%, compared with using climatological MLD; it provides only very limited improvement in T100, ~2%, while ~7% in T30 (Fig. 12e). Evidently the subsurface structure plays a bigger role in T100 than in UOHC.

d. Regional and TC-relevant performances

Given that the main purpose of SNAP is to aid hurricane forecasting, it is of interest to examine the regional performance of SNAP-derived quantities, especially in areas that are sensitive to hurricanes. Using the moving box (10° longitude by 5° latitude) technique

TABLE 2. Monthly RMSDs of 1D-PWP-derived MLD and NRL_MLD with respect to Argo_MLD. The differences and improved percentages both are relative to NRL_MLD's RMSD.

Month	RMSD of PWP's MLD (m)	RMSD of NRL's MLD (m)	Difference (m)	Improved (%)	Sample size
Jun	13.8	16.1	−2.3	14.6	2312
Jul	10.8	12.9	−2.1	16.3	2374
Aug	9.4	11.1	−1.7	15.6	2430
Sep	11.2	14.1	−2.9	20.3	2663
Oct	12.5	16.4	−3.9	23.7	2844
Nov	18.1	20.9	−2.8	13.5	2616

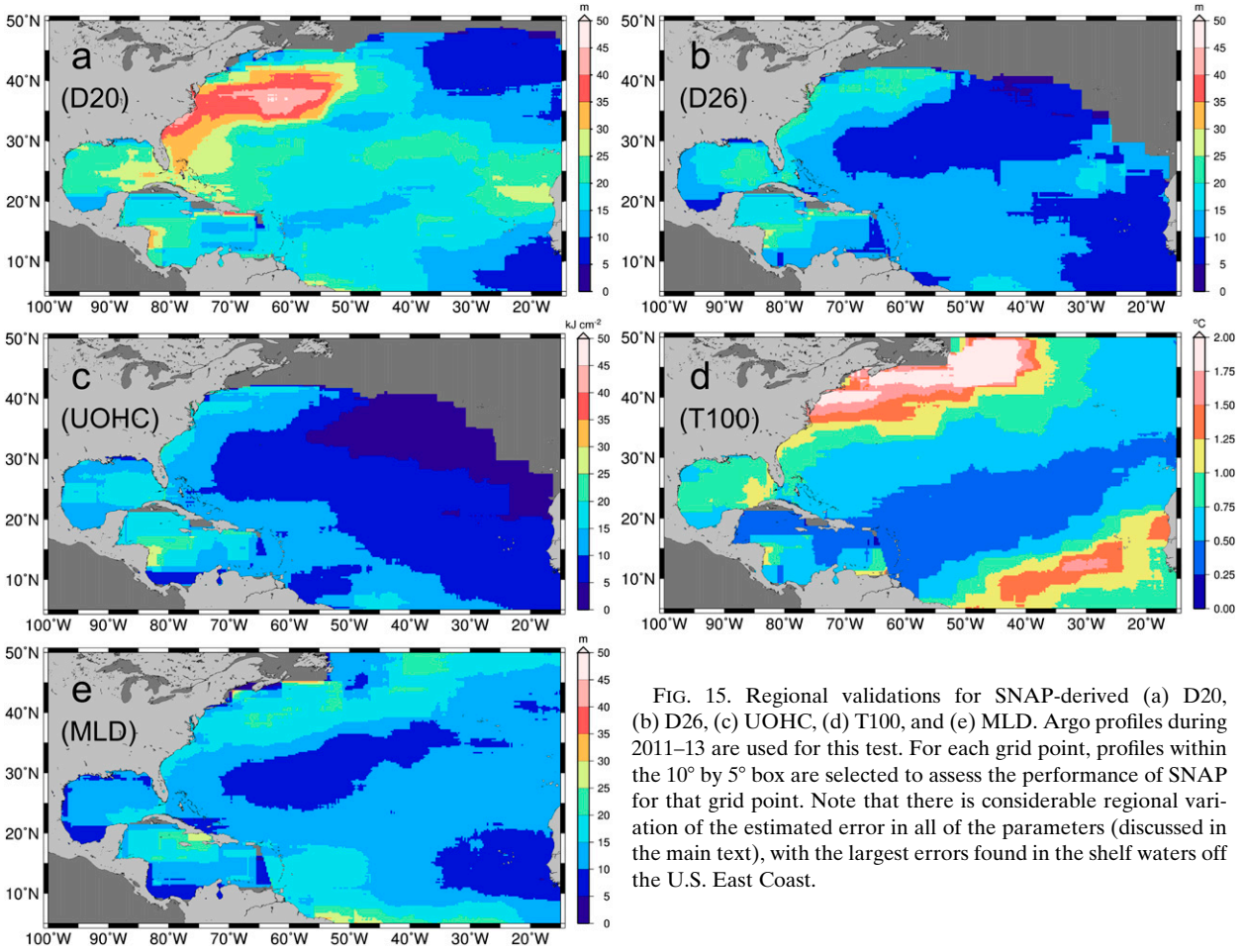

FIG. 15. Regional validations for SNAP-derived (a) D20, (b) D26, (c) UOHC, (d) T100, and (e) MLD. Argo profiles during 2011–13 are used for this test. For each grid point, profiles within the 10° by 5° box are selected to assess the performance of SNAP for that grid point. Note that there is considerable regional variation of the estimated error in all of the parameters (discussed in the main text), with the largest errors found in the shelf waters off the U.S. East Coast.

introduced in section 3a, regional validations for OTS parameters are conducted with the Argo profiles from 2011 to 2013 (Fig. 15).

The RMSDs are somewhat higher over the regions of the Loop Current (GOM) and the Gulf Stream compared to the overall performance (Fig. 15). Specifically, the SNAP-derived D20 has an RMSD = 25–30 m in the Loop Current and 30–40 m in the Gulf Stream (Fig. 15a). These are 20%–40% and 40%–90% higher than the RMSD for the NAO overall, 21.5 m. The errors are larger in these regions due to the high mesoscale variability over the GOM and over the Gulf Stream (Fig. 7a). Similar spatial patterns are found in the error estimates of D26 and UOHC (Figs. 15b,c). SNAP-derived T100 also exhibits greater uncertainties in these two regions (1.25°C and nearly 2°C in the Loop Current and in the Gulf Stream, respectively) and over the southeastern NAO (Fig. 15d). For 1D-PWP-derived MLD, relatively larger uncertainties (>20 m) appear in the Gulf Stream, the Caribbean Sea, and the southern NAO (Fig. 15e).

Still another and more relevant way to assess the performance of SNAP is to sample along actual TC tracks (Fig. 16). A subset of Argo profiles representing TC condition was extracted from the validation dataset based on the 6-hourly best track data during 2011–13 from the National Hurricane Center. Profiles within ±3 days and a radius of 2° latitude at each TC location were selected (Fig. 16a). This sampling indicates that the performance of SNAP under TC condition is as good as the performance for the NAO overall (Fig. 12 vs Figs. 16b–e).

e. Comparisons with a long-term Argo float

To further illustrate the performance of SNAP, a comparison is made between SNAP data and the temperature measurements from a long-lived Argo float 4901224, which reported the temperature profile every 10 days (Fig. 17). This float was deployed at 23.5°N, 71°W on 18 December 2010 and remained within the southern part of the North Atlantic Subtropical Gyre. The comparison period is from 27 December 2010 to 25 May 2013 covering two hurricane seasons: 2011 and

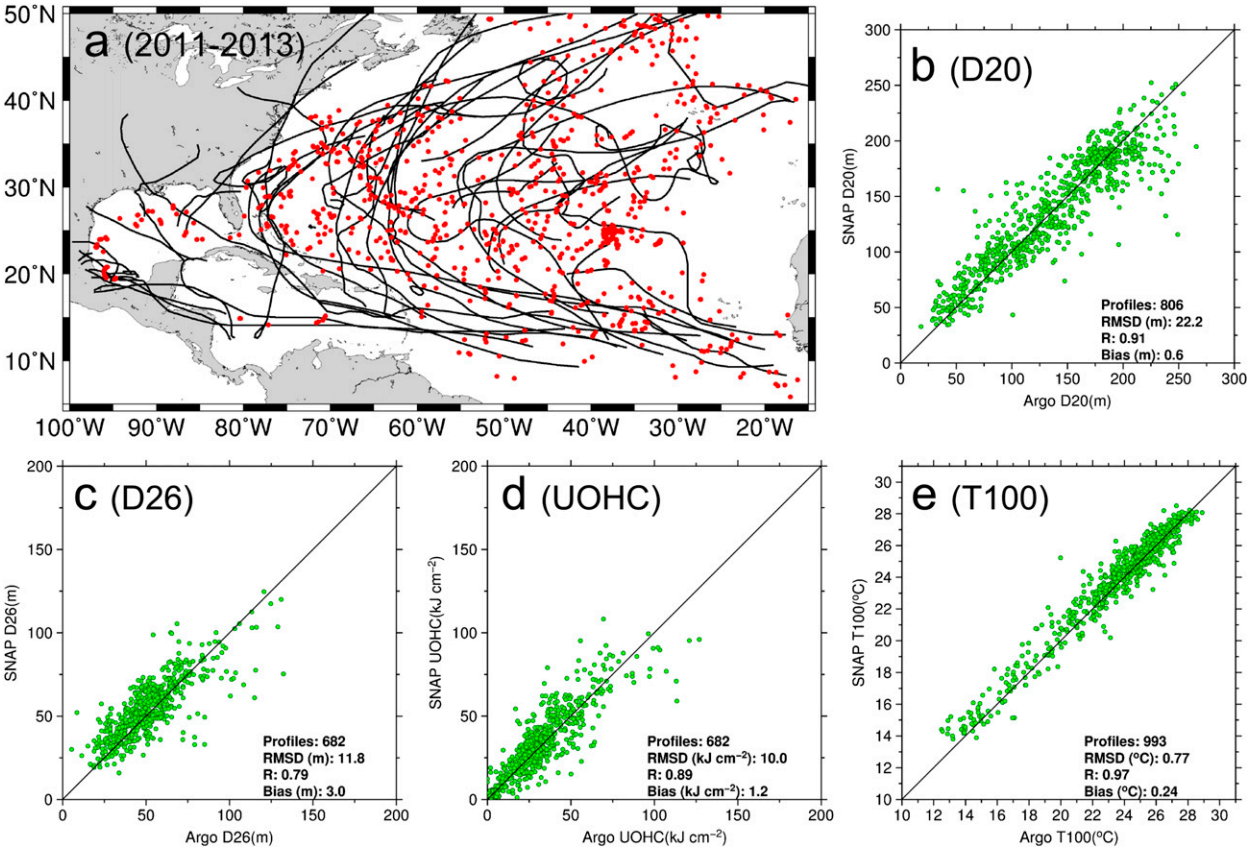

FIG. 16. (a) Argo profiles (red) within ±3 days and a radius of 2° latitude at each 6-hourly TC location during 2011–13. The hurricane tracks in (a) are obtained from the National Hurricane Center. SNAP-derived (b) D20, (c) D26, (d) UOHC, and (e) T100 are compared with the Argo observations in (a) to assess the performance of SNAP under TC condition. These results are similar to the NAO overall performance (Fig. 12).

2012. It is evident that SNAP-derived data are in generally good agreement with these Argo observations (Figs. 17a,b). The RMSD of four ocean parameters: D26, D20, UOHC, and T100 are 9 m, 23 m, 10.4 kJ cm^{-2}, and 0.4°C, respectively, (Figs. 17d–g), which are just slightly better (viz. in D26 and T100) than the performance for the NAO overall (cf. Fig. 12).

f. Comparison with an operational two-layer model

Today, most of the operational ocean parameters used for hurricane prediction are based on a two-layer model (Goni and Trinanes 2003; Mainelli et al. 2008; Shay and Brewster 2010; Meyers et al. 2014). It is interesting to compare the results derived from the two-layer model to see whether the new regression model provides better estimations. The accuracy of the NOAA's operational two-layer model over the NAO based on Shay et al. (2012) is shown in Table 3. It should be noted that the sample size for their validation is different from the one used in the present study, ~50 000 versus ~19 000 in the present study. The overall improvement made by SNAP in the RMSD of UOHC is about 30%. It is noteworthy that the RMSD of MLD is reduced by ~27% as compared to the previous approach, which estimates MLD from climatology and SSHA (just the way SNAP estimates isotherm depths; Shay et al. 2012; Meyers et al. 2014).

6. Discussion and conclusions

a. Relative contribution of SSHA, SST, and 1D-PWP-derived MLD

According to the algorithm shown in Fig. 11, SNAP consists of two main parts: 1) the surface mixed layer structure and 2) subsurface isotherm depths. The vertically integrated or averaged parameters, UOHC and T100, depend upon the entire upper-ocean profile, and so have contribution from both mixed layer structure based on SST and 1D-PWP-derived MLD and isotherm depths based on SSHA. It is interesting to examine the relative contribution of these components (i.e., SSHA, SST, and 1D-PWP-derived MLD) to UOHC and T100.

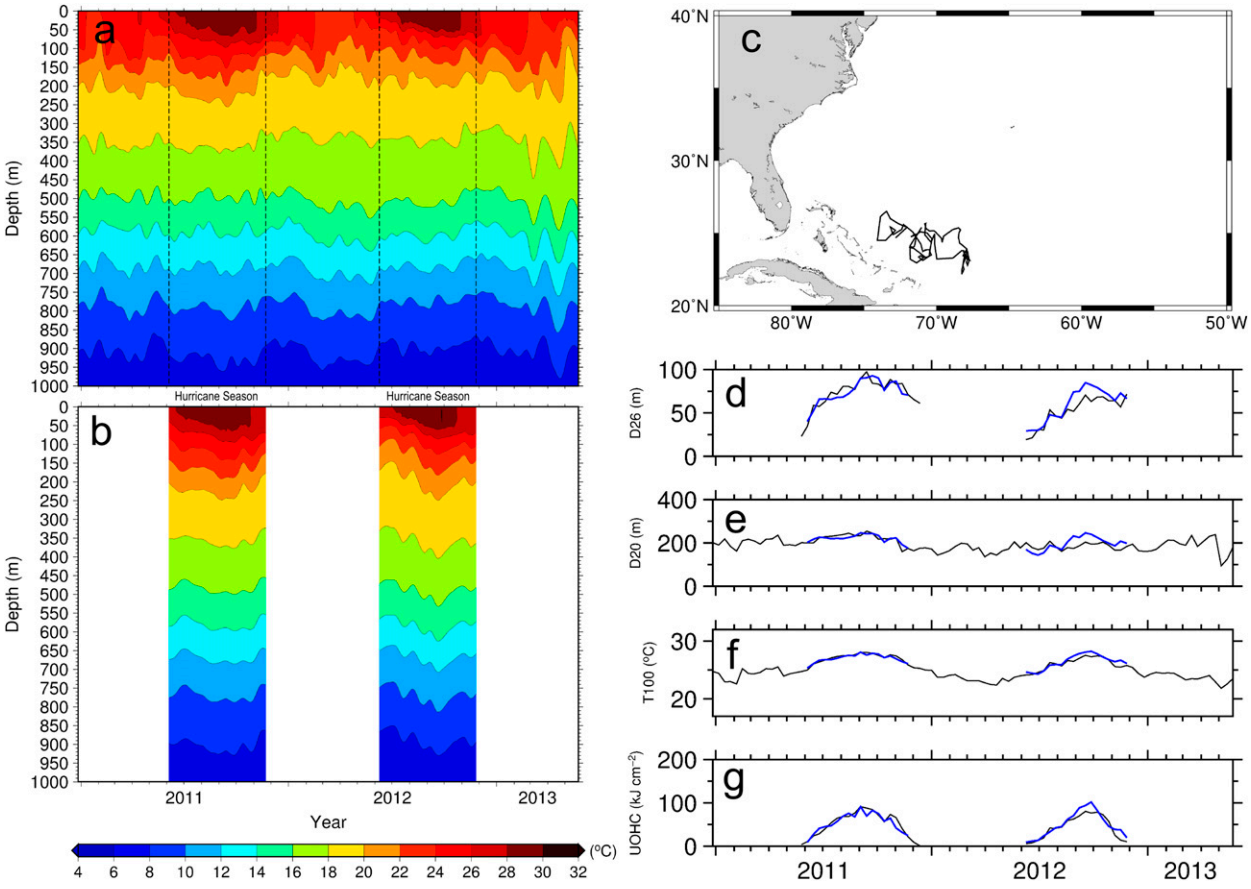

FIG. 17. Long-term comparison of SNAP estimated OTS with the Argo float 4901224. (a) Time series of temperature structure from surface to 1000 m observed by the float 4901224 from 27 Dec 2010 to 25 May 2013. (b) The corresponding time series from SNAP, and just the hurricane seasons. (c) The trajectory of the float 4901224. (d)–(g) Comparisons for D26, D20, T100, and UOHC. Black (blue) curve represents data from the float 4901224 (SNAP). In this comparison, RMSDs for D26, D20, T100, and UOHC are 9 m, 23 m, 0.4°C, and 10.4 kJ cm^{-2}, respectively, which are roughly the same as RMSD for the NAO overall (cf. Fig. 12).

To separate the contribution to SNAP from SST and SSHA, a reduced version of SNAP (hereafter SNAP_nosst) was generated using no MLD information whatsoever. As a reference, still another version was made using GDEM only (i.e., no SSHA information). This will be dubbed GDEM.

First UOHC is examined: SNAP and SNAP_nosst reduce the error by 13.5 kJ cm^{-2} (~58%) and 3.3 kJ cm^{-2} (~14%) respectively, compared to GDEM (Fig. 18). This indicates that there is only about a 24% (i.e., 3.3/13.5 kJ cm^{-2}) improvement contributed by SSHA, while a larger fraction, 76%, is due to SST and 1D-PWP-derived MLD. The relatively small effect of SSHA on UOHC is understandable, because the integration depth (down to D26) is generally closer to the surface, so that the mixed layer properties are of greatest importance. As for T100, SNAP reduces RMSD by 0.4°C (~33%) as compared to GDEM, whereas SNAP_nosst reduces RMSD by 0.2°C (~17%) (Fig. 18). Thus, SSHA contributes 50% (0.2°/0.4°C) toward improving the accuracy of T100, and the remainder comes from SST and 1D-PWP-dierved MLD. Of course, T100 takes

TABLE 3. Overall RMSDs (biases) of D20, D26, MLD, and UOHC from the two-layer model based on Shay et al. (2012) and from SNAP. Note that the sample sizes between Shay et al. (2012) and the present study are different; the former has ~50 000 profiles and the latter has 19 076 profiles.

	D20 (m)	D26 (m)	MLD (m)	UOHC (kJ cm^{-2})
Two-layer model	31.0 (−0.5)	18.2 (−8.4)	17.2 (−3.6)	15.0 (−3.0)
SNAP	21.5 (2.9)	12.0 (2.4)	12.6 (−3.7)	9.7 (1.9)

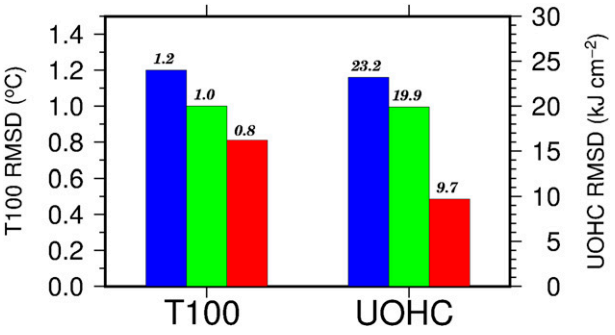

FIG. 18. Rms differences of T100 and UOHC with respect to Argo that follow from using GDEM climatology only (blue), from SNAP_nosst (no specific treatment of the surface layer, green), and from the full SNAP (red). As always, the Argo profiles used for this test are from June to November of 2011–13. Notice that the full SNAP result is significantly improved. The respective values are shown on the top of the bars.

the upper 100 m into account, which often exceeds the base of the mixed layer and hence the SSHA-derived isotherm depths play a critical role providing the information from greater depths.

b. *Error budget for SNAP estimations*

The goal of this study is to provide a near-real-time, high spatial resolution OTS field that would aid hurricane forecasting. It is noted that the goal for hurricane forecasting was an accuracy of 5 kJ cm^{-2} rms for UOHC and 0.5°C for T100. The accuracy of SNAP at its present stage is 10 kJ cm^{-2} and 0.8°C (Figs. 12c,d), and so there is clearly room for and a need for improvement. SNAP can be improved further by more in situ temperature profiles for the regressions, by better SST and MLD products, and by higher spatial resolution SSHA observations.

Of course, not even perfect SSHA would yield perfect estimations of OTS. Random noise associated with high-frequency fluctuations (e.g., tides or internal waves) of isotherm depth will always exist. Here this study attempts to determine the error budget from four possible sources: high-frequency fluctuations, intrinsic altimetric uncertainty (i.e., instrumental and mapping errors), barotropic (i.e., mass redistribution) components, and salinity effects. To assess the high-frequency fluctuation in the isotherm depths, this study makes use of the observation from a new profiling float, the Air-Launched Autonomous Micro Observer (ALAMO; http://alamo.whoi.edu/), which was specifically designed for hurricane research and which measures a temperature profile every 6 h. During August 2014–November 2015 in the North Atlantic around 16.5°N, 59°W, it is found that the high-frequency fluctuation is 4–6 m rms, for isotherms between D26 and D17 (blue line in Fig. 19a). This variation accounts for 16%–34% of the error of SNAP-derived isotherm depth estimates, which of course do not account for high-frequency variability in subsurface OTS.

The typical uncertainty in AVISO SSHA maps is ~3 cm. This will introduce a 3–10-m rms error in SNAP-derived isotherm depths D26-D17 (red line in Fig. 19a), accounting for 24%–33% of the total error.

To assess the barotropic and salinity contributions to error, this study takes advantage of the temperature

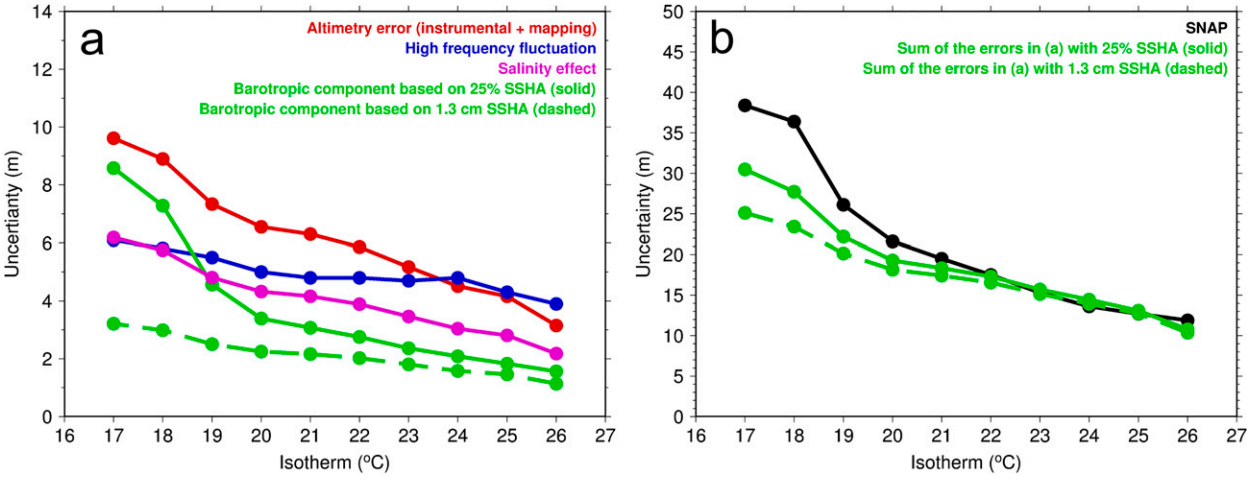

FIG. 19. (a) Individual uncertainties in SNAP-derived isotherm depth estimations from D26 to D17. They include altimetry error (red), high-frequency fluctuation (blue), salinity effect (magenta), and barotropic (or mass) component (green). For the barotropic assessment, two approaches are examined, which are based on Baker-Yeboah et al. (2009) (solid green) and the Argo float 4901224 (dashed green). (b) The rms errors of SNAP-derived isotherm depths (black) and the sum of the individual errors in (a). Solid green represents the sum with barotropic estimation from Baker-Yeboah et al. (2009) and dashed green represents the sum with barotropic estimation from the Argo float 4901224.

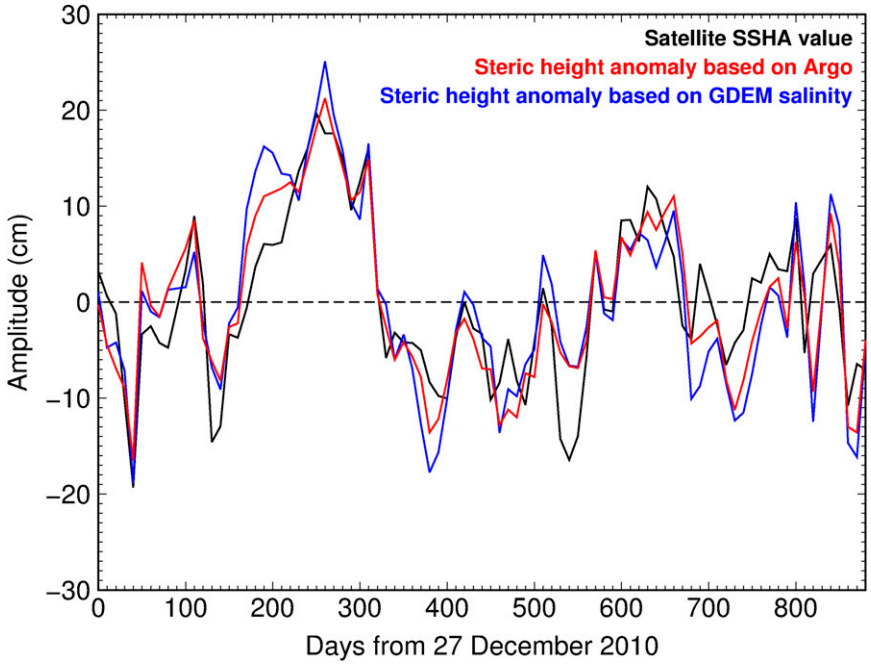

FIG. 20. Time series from 27 Dec 2010 to 25 May 2013 for steric height anomaly based on in situ temperature and salinity profile data from the Argo float 4901224 (red), steric height anomaly based on the Argo in situ temperature but GDEM climatological salinity (blue), and corresponding SSHA (black). The steric height is relative to 1000-m depth. The respective mean over the whole period is removed from steric height and SSHA. Note that the steric (baroclinic) component dominates the sea surface height signal.

and salinity profile data from the Argo float 4901224 (Fig. 17). First, the steric height referred to 1000-m depth is calculated from each temperature and salinity profile pair from 27 December 2010 to 25 May 2013, and the mean over the entire period is then removed to obtain the anomaly field (Fig. 20). A similar set of steric height anomaly series but with GDEM climatological salinity profile is generated to assess the salinity effect in the steric height. Second, the corresponding SSHA values are extracted from the SSHA maps and the period mean is also removed to be consistent with the steric height series.

From Fig. 20, it can be found that the variations of steric height anomaly are fairly consistent with that of SSHA, implying that the steric (baroclinic) component dominates the sea surface height signal. The rms difference between the steric height anomaly and SSHA is 4.3 cm, which is in good agreement with Gilson et al. (1998), who reported that RMSD is about 5.2 cm in the North Pacific Ocean based on 20 XBT historical transects. This difference between steric height anomaly and SSHA can likely be attributed to altimetry uncertainty, the barotropic component and the deep (below 1000 m) steric variation. If assuming that the deep steric variation is negligible, then the barotropic part accounts for about 1.3-cm RMSD (i.e., 4.3–3 cm), which would yield a 1–3-m uncertainty in SNAP-derived isotherm depth estimations, equivalent to 8%–12% of the overall error. Alternately, Baker-Yeboah et al. (2009) reported that the barotropic component can be up to 25% of the SSHA signal in the eastern South Atlantic Ocean. With this assumption (25% of SSHA is due to barotropic motions), the resulting rms error in SNAP-derived isotherm depths is roughly consistent with the result found from the Argo float data, except for D17 and D18 (green lines in Fig. 19a).

To estimate the salinity contribution, the steric height anomalies obtained from observed profiles and the ones substituted with GDEM climatological salinity profiles are compared. It is found that salinity contributes a 2.5-cm rms in steric height calculation, which is also consistent with the value found in the North Pacific Ocean (Gilson et al. 1998). This will lead to a 2–6-m rms error in SNAP-derived isotherm depth estimations (magenta line in Fig. 19a), accounting for 15%–21% of the overall error of SNAP-derived isotherm depths.

According to this error assessment, it is found that the largest error comes from altimetry uncertainty, then follows high-frequency fluctuations, then the salinity

TABLE 4. Comparison of the methods between PLK14 and SNAP.

	PLK14	SNAP
Region	WNPO	NAO
Profile sources	Argo	Argo, CTD, XBT
Profiles for regression	38 556	138 899
Climatology	Monthly WOA01	Daily GDEM
MLD	Monthly climatology	Daily from 1D-PWP

effect, and finally, the barotropic contribution to SSHA. These four factors explain most of the uncertainty in SNAP-derived isotherm depths (Fig. 19b). It should be noted, however, that the present assessment is relatively rough with a very limited dataset (one ALAMO float and one Argo float), and the likelihood is that the contribution of each component will have regional dependence.

c. *SNAP website*

Under a joint effort between National Taiwan University and Woods Hole Oceanographic Institution a web page (http://www.whoi.edu/science/PO/people/ipun/) has been established to distribute operational SNAP-derived temperature profiles along with fields of UOHC and T100. The data products on this website encompass both the NAO region described here, and the WNPO (PLK14). The operational SNAP product is nominally delivered in near–real time depending on SST and SSHA data streams.

d. *Summary and conclusions*

Upper-ocean thermal structure plays a critical role in controlling TC intensity, especially for the strongest storms and those that move slowly (Lin et al. 2014; Balaguru et al. 2015). It has been a significant challenge, even with today's ocean observing systems, to operationally monitor the subsurface temperature with a basin-wide coverage (Goni et al. 2009). Pioneering efforts by Goni et al. (1996) and Shay et al. (2000) made use of a two-layer model to derive synthetic ocean temperature profiles based on satellite-derived SSHA. This study follows PLK14's framework for estimating subsurface OTS, and adds on daily climatology and daily 1D-PWP-derived MLD (Table 4), to derive improved surface layer properties. The SNAP-derived UOHC and T100 are of useful accuracy with RMSDs of ~10 kJ cm^{-2} and ~0.8°C, respectively, though they have regional dependence and clearly there is room for improvement. One of the most important improvements in SNAP is making use of daily MLD estimated from the 1D-PWP. It is found that RMSD of 1D-PWP-derived MLD is ~13 m, which is equivalent to ~19% improvement with respect to NRL's climatological monthly MLD used in PLK14. There is roughly a ~30% overall improvement by SNAP as compared to the now widely used two-layer-derived parameters.

Although the immediate objective here was for hurricane forecasting applications, SNAP can also be applied to other issues related to the ocean subsurface thermal structure, such as the initialization of ocean models and long-term subsurface temperature change (Huang et al. 2015; Lin and Chan 2015). Based on satellite observation, Pun et al. (2013) reported that the ocean subsurface of the WNPO's typhoon main development region has warmed significantly in the past two decades. It is of great interest to examine whether a NAO counterpart may also be present.

Acknowledgments. The authors appreciate the Argo team for the in situ temperature profiles, the AVISO team for the SSHA maps, the RSS team for the SST products, NOAA/NODC for the in situ ocean temperature data, NRL for the climatological temperature and MLD data, and NOAA/NCEP for the surface reanalysis fields. The authors also like to acknowledge Dr. I. I. Lin for her valuable comments and suggestions. Finally, sincerely thanks to three anonymous reviewers for their insightful and constructive comments. IFP is supported by Grants NSC 101-2628-M-002-001-MY4 and MOST 103-2111-M-002 -002 -MY3. JFP and SRJ were supported by the U.S. Office of Naval Research under the project "Impact of Typhoons on the North Pacific, ITOP."

REFERENCES

Ali, M. M., D. Swain, and R. A. Weller, 2004: Estimation of ocean subsurface thermal structure from surface parameters: A neural network approach. *Geophys. Res. Lett.*, **31**, L20308, doi:10.1029/2004GL021192.

Baker-Yeboah, S., D. R. Watts, and D. A. Byrne, 2009: Measurements of sea surface height variability in the eastern South Atlantic from pressure sensor–equipped inverted echo sounders: Baroclinic and barotropic components. *J. Atmos. Oceanic Technol.*, **26**, 2593–2609, doi:10.1175/2009JTECHO659.1.

Balaguru, K., G. R. Foltz, L. R. Leung, E. D'Asaro, K. A. Emanuel, H. Liu, and S. E. Zedler, 2015: Dynamic potential intensity: An improved representation of the ocean's impact on tropical cyclones. *Geophys. Res. Lett.*, **42**, 6739–6746, doi:10.1002/2015GL064822.

Bender, M. A., and I. Ginis, 2000: Real-case simulations of hurricane–ocean interaction using a high-resolution coupled model: Effects on hurricane intensity. *Mon. Wea. Rev.*, **128**, 917–946, doi:10.1175/1520-0493(2000)128<0917:RCSOHO>2.0.CO;2.

——, ——, and Y. Kurihara, 1993: Numerical simulations of tropical cyclone–ocean interaction with a high-resolution coupled model. *J. Geophys. Res.*, **98**, 23 245–23 263, doi:10.1029/93JD02370.

Bernie, D. J., S. J. Woolnough, J. M. Slingo, and E. Guilyardi, 2005: Modeling diurnal and intraseasonal variability of the ocean mixed layer. *J. Climate*, **18**, 1190–1202, doi:10.1175/JCLI3319.1.

Boyer, T. P., and Coauthors, 2009: Introduction. *World Ocean Database 2009*, NOAA Atlas NESDIS 66, 216 pp.

Carnes, M. R., 2009: Description and evaluation of GDEM-V3.0. NRL Memo. Rep. NRL/MR/7330-09-9165, 24 pp.

——, J. L. Mitchell, and P. W. Dewitt, 1990: Synthetic temperature profiles derived from Geosat altimetry—Comparison with air-dropped expendable bathythermograph profiles. *J. Geophys. Res.*, **95**, 17 979–17 992, doi:10.1029/JC095iC10p17979.

Cione, J. J., 2015: The relative roles of the ocean and atmosphere as revealed by buoy air–sea observations in hurricanes. *Mon. Wea. Rev.*, **143**, 904–913, doi:10.1175/MWR-D-13-00380.1.

——, and E. Uhlhorn, 2003: Sea surface temperature variability in hurricanes: Implications with respect to intensity change. *Mon. Wea. Rev.*, **131**, 1783–1796, doi:10.1175//2562.1.

——, P. G. Black, and S. H. Houston, 2000: Surface observations in the hurricane environment. *Mon. Wea. Rev.*, **128**, 1550–1561, doi:10.1175/1520-0493(2000)128<1550:SOITHE>2.0.CO;2.

——, E. A. Kalina, J. A. Zhang, and E. W. Uhlhorn, 2013: Observations of air–sea interaction and intensity change in hurricanes. *Mon. Wea. Rev.*, **141**, 2368–2382, doi:10.1175/MWR-D-12-00070.1.

D'Asaro, E. A., and Coauthors, 2014: Impact of typhoons on the ocean in the Pacific. *Bull. Amer. Meteor. Soc.*, **95**, 1405–1418, doi:10.1175/BAMS-D-12-00104.1.

Ducet, N., P. Y. Le Traon, and G. Reverdin, 2000: Global high-resolution mapping of ocean circulation from TOPEX/Poseidon and ERS-1 and-2. *J. Geophys. Res.*, **105**, 19 477–19 498, doi:10.1029/2000JC900063.

Emanuel, K. A., 1986: An air–sea interaction theory for tropical cyclones. Part I: Steady-state maintenance. *J. Atmos. Sci.*, **43**, 585–605, doi:10.1175/1520-0469(1986)043<0585:AASITF>2.0.CO;2.

——, 1999: Thermodynamic control of hurricane intensity. *Nature*, **401**, 665–669, doi:10.1038/44326.

——, C. DesAutels, C. Holloway, and R. Korty, 2004: Environmental control of tropical cyclone intensity. *J. Atmos. Sci.*, **61**, 843–858, doi:10.1175/1520-0469(2004)061<0843:ECOTCI>2.0.CO;2.

Fox, D. N., W. J. Teague, C. N. Barron, M. R. Carnes, and C. M. Lee, 2002: The Modular Ocean Data Assimilation System (MODAS). *J. Atmos. Oceanic Technol.*, **19**, 240–252, doi:10.1175/1520-0426(2002)019<0240:TMODAS>2.0.CO;2.

Fu, L. L., E. J. Christensen, C. A. Yamarone, M. Lefebvre, Y. Menard, M. Dorrer, and P. Escudier, 1994: TOPEX/POSEIDON mission overview. *J. Geophys. Res.*, **99**, 24 369–24 381, doi:10.1029/94JC01761.

Gallacher, P. C., R. Rotunno, and K. A. Emanuel, 1989: Tropical cyclogenesis in a coupled ocean-atmosphere model. Preprints, *18th Conf. on Hurricanes and Tropical Meteorology*, San Diego, CA, Amer. Meteor. Soc., 121–122.

Gentemann, C. L., T. Meissner, and F. J. Wentz, 2010: Accuracy of satellite sea surface temperatures at 7 and 11 GHz. *IEEE T. Geosci. Remote*, **48**, 1009–1018, doi:10.1109/TGRS.2009.2030322.

Gilson, J., D. Roemmich, B. Cornuelle, and L. L. Fu, 1998: Relationship of TOPEX/Poseidon altimetric height to steric height and circulation in the North Pacific. *J. Geophys. Res.*, **103**, 27 947–27 965, doi:10.1029/98JC01680.

Goni, G., and J. A. Trinanes, 2003: Ocean thermal structure monitoring could aid in the intensity forecast of tropical cyclones. *Eos, Trans. Amer. Geophys. Union*, **84**, 573–580, doi:10.1029/2003EO510001.

——, S. Kamholz, S. Garzoli, and D. Olson, 1996: Dynamics of the Brazil-Malvinas Confluence based on inverted echo sounders and altimetry. *J. Geophys. Res.*, **101**, 16 273–16 289, doi:10.1029/96JC01146.

——, and Coauthors, 2009: Applications of satellite-derived ocean measurements to tropical cyclone intensity forecasting. *Oceanography*, **22**, 190–197, doi:10.5670/oceanog.2009.78.

Gould, J., and Coauthors, 2004: Argo profiling floats bring new era of in situ ocean observations. *Eos, Trans. Amer. Geophys. Union*, **85**, 185–191, doi:10.1029/2004EO190002.

Guinehut, S., A.-L. Dhomps, G. Larnicol, and P.-Y. Le Traon, 2012: High resolution 3-D temperature and salinity fields derived from in situ and satellite observations. *Ocean Sci.*, **8**, 845–857, doi:10.5194/os-8-845-2012.

Hong, X. D., S. W. Chang, S. Raman, L. K. Shay, and R. Hodur, 2000: The interaction between Hurricane Opal (1995) and a warm core ring in the Gulf of Mexico. *Mon. Wea. Rev.*, **128**, 1347–1365, doi:10.1175/1520-0493(2000)128<1347:TIBHOA>2.0.CO;2.

Huang, P., I. I. Lin, C. Chou, and R. H. Huang, 2015: Change in ocean subsurface environment to suppress tropical cyclone intensification under global warming. *Nat. Commun.*, **6**, 7188, doi:10.1038/ncomms8188.

Jacob, S. D., L. K. Shay, A. J. Mariano, and P. G. Black, 2000: The 3D mixed layer response to Hurricane Gilbert. *J. Phys. Oceanogr.*, **30**, 1407–1429, doi:10.1175/1520-0485(2000)030<1407:TOMLRT>2.0.CO;2.

Jaimes, B., and L. K. Shay, 2009: Mixed layer cooling in mesoscale oceanic eddies during hurricanes Katrina and Rita. *Mon. Wea. Rev.*, **137**, 4188–4207, doi:10.1175/2009MWR2849.1.

——, ——, and E. W. Uhlhorn, 2015: Enthalpy and momentum fluxes during Hurricane Earl relative to underlying ocean features. *Mon. Wea. Rev.*, **143**, 111–131, doi:10.1175/MWR-D-13-00277.1.

Kantha, L. H., and C. A. Clayson, 1994: An improved mixed layer model for geophysical applications. *J. Geophys. Res.*, **99**, 25 235–25 266, doi:10.1029/94JC02257.

Kara, A. B., P. A. Rochford, and H. E. Hurlburt, 2002: Naval Research Laboratory mixed layer depth (NMLD) climatologies. NRL Rep. NRL/FR/7330-02-9995, 26 pp.

——, ——, and ——, 2003: Mixed layer depth variability over the global ocean. *J. Geophys. Res.*, **108**, 3079, doi:10.1029/2000JC000736.

Klemas, V., and X. H. Yan, 2014: Subsurface and deeper ocean remote sensing from satellites: An overview and new results. *Prog. Oceanogr.*, **122**, 1–9, doi:10.1016/j.pocean.2013.11.010.

Ko, D. S., S. Y. Chao, C. C. Wu, and I. I. Lin, 2014: Impacts of Typhoon Megi (2010) on the South China Sea. *J. Geophys. Res.*, **119**, 4474–4489, doi:10.1002/2013JC009785.

Kosaka, Y., 2014: Increasing wind sinks heat. *Nat. Climate Change*, **4**, 172–173, doi:10.1038/nclimate2138.

Leipper, D. F., and D. Volgenau, 1972: Hurricane heat potential of the Gulf of Mexico. *J. Phys. Oceanogr.*, **2**, 218–224, doi:10.1175/1520-0485(1972)002<0218:HHPOTG>2.0.CO;2.

Lin, I. I., and Coauthors, 2013: An ocean cooling potential intensity index for tropical cyclones. *Geophys. Res. Lett.*, **40**, 1878–1882, doi:10.1002/grl.50091.

——, and J. Chan, 2015: Recent decrease in typhoon destructive potential and global warming implications. *Nat. Commun.*, **6**, 7182, doi:10.1038/ncomms8182.

——, C. C. Wu, K. A. Emanuel, I. H. Lee, C. R. Wu, and I. F. Pun, 2005: The interaction of Supertyphoon Maemi (2003) with a

warm ocean eddy. *Mon. Wea. Rev.*, **133**, 2635–2649, doi:10.1175/MWR3005.1.

——, ——, I. F. Pun, and D. S. Ko, 2008: Upper-ocean thermal structure and the western North Pacific category-5 typhoons. Part I: Ocean features and the category-5 typhoons' intensification. *Mon. Wea. Rev.*, **136**, 3288–3306, doi:10.1175/2008MWR2277.1.

——, I. F. Pun, and C. C. Wu, 2009: Upper-ocean thermal structure and the western North Pacific category-5 typhoons. Part II: Dependence on translation speed. *Mon. Wea. Rev.*, **137**, 3744–3757, doi:10.1175/2009MWR2713.1.

——, ——, and C. C. Lien, 2014: "Category-6" supertyphoon Haiyan in global warming hiatus: Contribution from subsurface ocean warming. *Geophys. Res. Lett.*, **41**, 8547–8553, doi:10.1002/2014GL061281.

Mainelli, M., M. DeMaria, L. K. Shay, and G. Goni, 2008: Application of oceanic heat content estimation to operational forecasting of recent Atlantic category 5 hurricanes. *Wea. Forecasting*, **23**, 3–16, doi:10.1175/2007WAF2006111.1.

Mellor, G. L., and T. Yamada, 1982: Development of a turbulence closure-model for geophysical fluid problems. *Rev. Geophys.*, **20**, 851–875, doi:10.1029/RG020i004p00851.

Meyers, P. C., L. K. Shay, and J. K. Brewster, 2014: Development and analysis of the systematically merged Atlantic regional temperature and salinity climatology for oceanic heat content estimates. *J. Atmos. Oceanic Technol.*, **31**, 131–149, doi:10.1175/JTECH-D-13-00100.1.

Pascual, A., Y. Faugere, G. Larnicol, and P. Y. Le Traon, 2006: Improved description of the ocean mesoscale variability by combining four satellite altimeters. *Geophys. Res. Lett.*, **33**, L02611, doi:10.1029/2005GL024633.

——, C. Boone, G. Larnicol, and P. Y. Le Traon, 2009: On the quality of real-time altimeter gridded fields: Comparison with in situ data. *J. Atmos. Oceanic Technol.*, **26**, 556–569, doi:10.1175/2008JTECHO556.1.

Powell, M. D., P. J. Vickery, and T. A. Reinhold, 2003: Reduced drag coefficient for high wind speeds in tropical cyclones. *Nature*, **422**, 279–283, doi:10.1038/nature01481.

Price, J. F., 1981: Upper ocean response to a hurricane. *J. Phys. Oceanogr.*, **11**, 153–175, doi:10.1175/1520-0485(1981)011<0153:UORTAH>2.0.CO;2.

——, 2009: Metrics of hurricane-ocean interaction: Vertically-integrated or vertically-averaged ocean temperature? *Ocean Sci.*, **5**, 351–368, doi:10.5194/os-5-351-2009.

——, R. A. Weller, and R. Pinkel, 1986: Diurnal cycling: Observations and models of the upper ocean response to diurnal heating, cooling, and wind mixing. *J. Geophys. Res.*, **91**, 8411–8427, doi:10.1029/JC091iC07p08411.

Pun, I. F., I. I. Lin, C. R. Wu, D. H. Ko, and W. T. Liu, 2007: Validation and application of altimetry-derived upper ocean thermal structure in the western North Pacific Ocean for typhoon-intensity forecast. *IEEE Geosci. Remote Sens.*, **45**, 1616–1630, doi:10.1109/TGRS.2007.895950.

——, ——, and M. H. Lo, 2013: Recent increase in high tropical cyclone heat potential area in the Western North Pacific Ocean. *Geophys. Res. Lett.*, **40**, 4680–4684, doi:10.1002/grl.50548.

——, ——, and D. S. Ko, 2014: New generation of satellite-derived ocean thermal structure for the Western North Pacific typhoon intensity forecasting. *Prog. Oceanogr.*, **121**, 109–124, doi:10.1016/j.pocean.2013.10.004.

Roemmich, D., S. Riser, R. Davis, and Y. Desaubies, 2004: Autonomous profiling floats: Workhorse for broad-scale ocean observations. *Mar. Technol. Soc. J.*, **38**, 21–29, doi:10.4031/002533204787522802.

Sanford, T. B., P. G. Black, J. R. Haustein, J. W. Feeney, G. Z. Forristall, and J. F. Price, 1987: Ocean response to a hurricane. Part I: Observations. *J. Phys. Oceanogr.*, **17**, 2065–2083, doi:10.1175/1520-0485(1987)017<2065:ORTAHP>2.0.CO;2.

Schade, L. R., and K. A. Emanuel, 1999: The ocean's effect on the intensity of tropical cyclones: Results from a simple coupled atmosphere–ocean model. *J. Atmos. Sci.*, **56**, 642–651, doi:10.1175/1520-0469(1999)056<0642:TOSEOT>2.0.CO;2.

Shay, L. K., and E. W. Uhlhorn, 2008: Loop current response to Hurricanes Isidore and Lili. *Mon. Wea. Rev.*, **136**, 3248–3274, doi:10.1175/2007MWR2169.1.

——, and J. K. Brewster, 2010: Oceanic heat content variability in the eastern Pacific Ocean for hurricane intensity forecasting. *Mon. Wea. Rev.*, **138**, 2110–2131, doi:10.1175/2010MWR3189.1.

——, P. G. Black, A. J. Mariano, J. D. Hawkins, and R. L. Elsberry, 1992: Upper ocean response to Hurricane Gilbert. *J. Geophys. Res.*, **97**, 20 227–20 248, doi:10.1029/92JC01586.

——, G. J. Goni, and P. G. Black, 2000: Effects of a warm oceanic feature on Hurricane Opal. *Mon. Wea. Rev.*, **128**, 1366–1383, doi:10.1175/1520-0493(2000)128<1366:EOAWOF>2.0.CO;2.

——, J. K. Brewster, and E. Maturi, 2012: Algorithm theoretical basis document for ocean heat content version 1.0. Satellite Products and Services Review Board, NOAA/RSMAS, 32 pp.

Walker, N. D., R. R. Leben, and S. Balasubramanian, 2005: Hurricane-forced upwelling and chlorophyll *a* enhancement within cold-core cyclones in the Gulf of Mexico. *Geophys. Res. Lett.*, **32**, L18610, doi:10.1029/2005GL023716.

——, ——, C. T. Pilley, M. Shannon, D. C. Herndon, I. F. Pun, I. I. Lin, and C. L. Gentemann, 2014: Slow translation speed causes rapid collapse of northeast Pacific Hurricane Kenneth over cold core eddy. *Geophys. Res. Lett.*, **41**, 7595–7601, doi:10.1002/2014GL061584.

Willis, J. K., D. Roemmich, and B. Cornuelle, 2003: Combining altimetric height with broadscale profile data to estimate steric height, heat storage, subsurface temperature, and sea-surface temperature variability. *J. Geophys. Res.*, **108**, 3292, doi:10.1029/2002JC001755.

Wong, A., R. Keeley, and T. Carval, and the Argo Data Management Team, 2012: Argo quality control manual, version 2.7. Argo, 47 pp.

Wu, C. C., C. Y. Lee, and I. I. Lin, 2007: The effect of the ocean eddy on tropical cyclone intensity. *J. Atmos. Sci.*, **64**, 3562–3578, doi:10.1175/JAS4051.1.

Wu, X., X. H. Yan, Y. H. Jo, and W. T. Liu, 2012: Estimation of subsurface temperature anomaly in the North Atlantic using a self-organizing map neural network. *J. Atmos. Oceanic Technol.*, **29**, 1675–1688, doi:10.1175/JTECH-D-12-00013.1.